Kinematic Studies in the Search for a Low-Mass CP-Odd Higgs Boson for Mass Hypotheses in the Range from 20 GeV to 80 GeV

Jakob Walter

Besondere Lernleistung

Gymnasium Luisenstift
supervising teacher: Christian Pätzold
external supervisor: Manuel Gutsche
Radebeul, 20.12.2024

Contents

1 Introduction

In the year 2012 the Higgs boson was discovered by the LHC at CERN, after being postulated for over 45 years. The discovery was a significant event which further strengthened the Standard Model of particle physics (SM), which is to this day one of the most successful theories in physics [13]. However, there are still inconsistencies between the theoretical predictions of the SM and the experimental measurements. Since no experiment was able to prove the SM wrong, many believe that it is incomplete. This resulted in multiple theories being developed which postulate physics beyond the SM. The Two-Higgs-Doublet Model (2HDM) is one of those theories [21]. It attempts to resolve the derivations between the experimental and theoretical value of the anomalous magnetic momentum of the muon. Since this theory predicts the existence of multiple Higgs bosons, discovering one of them would strongly hint towards this theory being correct. This thesis is focused on the search for a low-mass CP-odd Higgs boson (A boson), which was predicted by the 2HDM for mass hypotheses in the range between 20 GeV and 80 GeV. The goal is to present multiple cuts that improve the significance of the A boson signal and therefore its upper limit. This cut optimization was done with masses calculated by a collinear mass approximation (COLL) as well as with the Missing Mass Calculator (MMC). It is based on the work and help of the working group for experimental particle physics at the IKTP at TU Dresden, who carried out the search for the A boson.
This work is structured as follows: In chapter 2 the theoretical background is explained while in chapter 3 the experimental setup is described. Chapter 4 talks about data, statistics and methods to reconstruct the invariant mass of the A boson. In chapter 5 the base analyses is introduced. Chapter 6 then presents the different cuts which improve the significance of the signal and therefore the upper limit of the signal strength. Finally a summary is given in chapter 7.

2 Theoretical Background

2.1 The Standard Model of Particle Physics

The SM of particle physics explains the strong, weak and electromagnetic force as well as all the elementary particles discovered to this day (figure 2.1). It is a quantum field theory, which combines classical field theory, special relativity and quantum mechanics.
Each mentioned fundamental force has an associated particle called a boson. The massless photon is the boson associated with the electromagnetic force. For the weak force three bosons exist, the charged W^+ and W^- and the neutral Z. Corresponding to the strong force gluons exists.
Apart from these spin-1 bosons, another boson, the spin-0 Higgs boson, exists. The spin is referring to an intrinsic form of an angular moment.
The rest of the SM consists of fermions, which can be divided into leptons and quarks. All of them have a spin of $\frac{1}{2}$. The leptons are able to interact via the weak force and if they have an electric charge additionally via the electromagnetic force. The electron (e^-), muon (μ^-) and tau-lepton (τ^-) are the charged leptons with an electric charge of -1, unlike the neutrinos which do not carry any electric charge and are different through their flavor (e, μ or τ) from each other. Each of those leptons has a corresponding antiparticle, with the same mass, same spin but opposite charges.
The electron, the positron (e^+) and the neutrinos are the only stable leptons. The muon and tau with their antiparticles are only different from the electron and positron by their masses and finite lifespan. All fermions are categorized into three families based on their properties, with each generation containing a charged lepton and its associated neutrino, along with two quarks with different electric charges. Quarks are the only type of elementary particles to interact with the three mentioned fundamental forces. They contain an electric charge of either $\frac{2}{3}e$ or $-\frac{1}{3}e$ and a colour charge. There are in total six different flavours of quarks with up and down being the lightest and only stable ones. Charm and strange as well as top and bottom decay into up and down to become stable. For each of the quarks exists an antiparticle with a colour charge of cyan, magenta or yellow. The flavours of quarks are not preserved, they can change via the weak force [29].

2.2 The Fundamental Forces

The Electromagnetic Force

The electromagnetic force is the best understood fundamental force with its source being the electric charge. Since this charge can be positive or negative, the force between two particles can either be attractive or repulsive. It is attractive if the particles are oppositely charged and repulsive if they have the same charge. The photon, as already mentioned, is the corresponding boson and has an infinite lifespan and no mass [22].

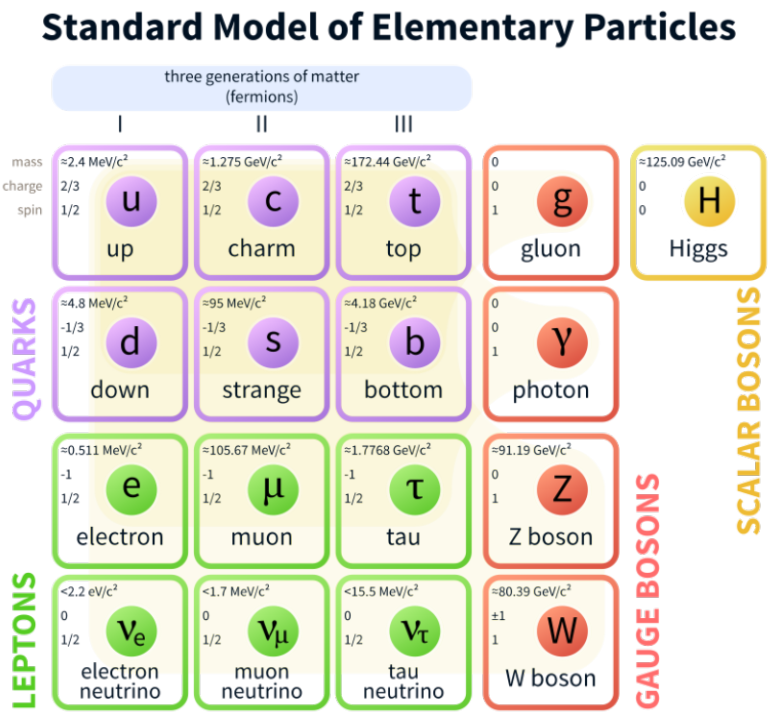

Figure 2.1: Overview on the particle content of the SM [17].

The Strong Force

The strong force is responsible for binding quarks together into protons or neutrons. On a slightly larger scale it confines the protons and neutrons in atomic nuclei. The corresponding bosons, as mentioned above, are the gluons. Gluons carry a colour charge, so in total eight independent types exist [22].
Since the strong force becomes stronger as quarks move apart, they are never found in isolation but instead are confined within larger particles called hadrons [3]. On the other hand the coupling constant (which determines the strength of the interaction) of the quarks decreases, as the distance between them becomes smaller. This leads to the quarks behaving like free particles when they are extremely close to each other. This is called asymptotic freedom [34]. When these hadronized quarks are produced in a decay and travel in approximately the same direction as the original quarks they are categorized as "jets". The particles in a jet are produced within narrow cones [33].

The Weak Force

The weak force plays a crucial role in particle decays. A prominent example for this is the beta-minus decay. It is responsible for changing an up-quark into a down-quark, which changes a proton into a neutron. Furthermore neutrinos only interact with other particles via the weak force and gravity. The weakness of this force leads to the neutrinos being difficult to detect [22]. Since the bosons of this force carry mass (W^+ and W^- with $m_W \approx 80$ GeV and Z with $m_Z \approx 90$ GeV), the weak force has a short range of about 10^{-3} fm.

The bosons of this force carry mass, which means that they are not stable and decay into other particles. One prominent decay channel of the Z boson is the $Z \to \tau\tau$ decay, in which the Z boson decays into two τ-leptons [29].

Gravitation

Gravitation as previous stated is the only fundamental force which cannot be explained by the SM, which also means that to this day no corresponding particle (graviton) has been found. The source of this force on a non-relativistic level is mass. Since the mass cannot be negative, this force is always attractive [22].

2.3 Invariant Mass

The invariant mass of a particle is based on the equivalence of energy and mass. The energy E of a particle can be calculated with the momentum p, the rest mass m and the speed of light c [22]:

$$E^2 = p^2c^2 + m^2c^4$$

In particle physics natural units are used in calculations. For the speed of light $c = 1$ is used, which simplifies the equation:

$$E^2 = p^2 + m^2$$

This leads to the invariant mass being calculated as follows:

$$m = \sqrt{E^2 - p^2}$$

2.4 Symmetries in Physics

In physics, symmetries are the most fundamental explanation of occurring phenomena. They describe a transformation under which a system stays the same. Most of the time conservation rules, like the conservation of energy or electric charge point towards a symmetry [22].

Parity Symmetry

Parity, also known as space inversion, refers to the transformation of a system by reflecting it through the origin of a coordinate system. If no transformations occur, then the system is p symmetric. This can apply to various systems, including the wave function of a particle, resulting in a mirror like reflection. It is denoted by P [22].

Charge Conjugation Symmetry

If a particle is interchanged with its corresponding anti particle and the laws of physics stay the same, then the system is symmetric under the charge conjugation symmetry. From this follows that the by the laws of physics predicted behavior of a particle is the same as for its anti particle. This symmetry is denoted by C [22].

CP Violation

The charge conjugation symmetry and the parity symmetry can be combined in the charged conjugation parity symmetry (CP-symmetry). This leads to a particle being CP-odd, when it violates this symmetry.
In a decay of an CP-odd particle into a τ-lepton pair a different angle between the decay planes of the two leptons can be measured, than in a decay of an CP-even particle. This means that CP-symmetry has a direct influence on the angular distance ΔR between two leptons. This also leads to the visible decay products of decaying CP-odd particles being more parallel than in CP-even decays [27].

2.5 The Higgs Mechanism

The electromagnetic force and the weak force can be combined in the electroweak unification. However, in this mathematical description, all elementary particles are without mass. This is not consistent with the experimental observations of those particles. To solve this inconsistency, P. Higgs, F. Englert and R. Brout introduced the Higgs mechanism in 1964. From this mechanism results a Higgs field which fills out all of space and a corresponding Higgs potential that defines the energy of the field as a function of its value. Since the potential is shaped like a well (Figure 2.2), it leads to the Higgs field having a non-zero vacuum expectation value (VEV). The vacuum state is the state in which the field has the lowest possible energy and the VEV is the average value of a quantum field in the vacuum. In this case the value is not zero, but around 246 GeV.
To gain mass the particles couple to the Higgs field. The stronger the coupling between a particle and the Higgs field's vacuum expectation value (VEV), the more massive the particle becomes. This means particles with greater masses have a stronger coupling to the Higgs field and, consequently, interact more intensely with the Higgs boson, which represents the excitation of the Higgs field. Both gauge bosons and fermions generate their masses from the Higgs mechanism, but each trough different processes [9].

2.6 Weaknesses of the Standard Model

The SM is one of the most successful theories in physics which means, that it can explain almost all interactions and processes observed around elementary particles. Still there are multiple observations and aspects that cannot be explained with the SM as it is today. One aspect, as previous stated, is that it only combines three of the four fundamental

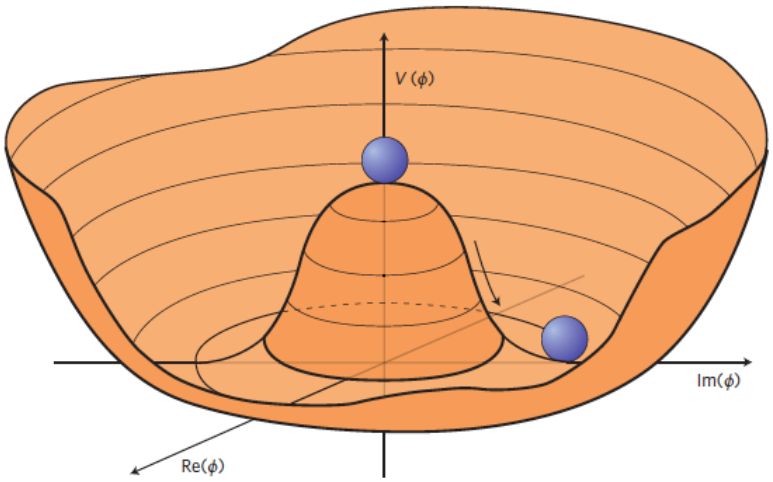

Figure 2.2: The higgs potential [16].

forces. Even though the gravitational force seems not to be relevant in particle physics, there have been many attempts to unify the gravitational force with the other three forces [22].
Furthermore there is an imbalance of matter and anti-matter in our universe, despite theories suggesting they should have been created in equal amounts during the Big Bang. This phenomenon is called the baryon asymmetry [24].
Another aspect the SM is not able to explain, is the occurrence of dark matter. Its impact can be seen while looking at the velocity of stars, which rotate around their galaxies. The observed velocity can only be explained if, apart from the visible matter, another type exists. It appears that this kind of matter only interacts over the gravitational force, which is why it is called dark matter. The limited interactions of dark matter make it difficult to explain. In total, more than six times more dark matter than regular matter exists in our universe [18].
Therefore multiple theories are being developed that try to expand or complete the physics beyond SM, such as supersymmetry and string theory.

Anomalous Magnetic Moment of the Muon

Important for this thesis is the anomalous magnetic moment of the muon a_μ, since the prediction of the SM for it differs greatly from the experimentally observed value. The magnetic moment $\vec{\mu}$ is a combined measure of how strong a magnetic source is and its orientation. It can be calculated using the g-factor g (quantification of how a particle's magnetic moment relates to its classical moment), which is predicted as $g = 2$, by the Dirac equation. This value does not take the effects of quantum electro dynamics into account, which leads to the observed value being different. The deviation is called the anomalous magnetic moment a and can be calculated as follows [8]:

$$a = \frac{(g-2)}{2}$$

The theoretical value of the anomalous moment of the muon has been calculated with the SM and amounts to [5]:

$$a_\mu^{\mathrm{SM}} = 116591810(43) \times 10^{-11}$$

It has also been measured by multiple experiments [2]. The average value of the combined results is:

$$a_\mu^{\mathrm{exp}} = 116592059(22) \times 10^{-11}$$

The comparison of the SM predicted value and the observed value leads to a discrepancy of up to 5 standard deviations [8]. One approach to explain this difference is done by using QCD lattice calculations. These calculations determine the contributions of the strong force to the anomalous moment of the muon. The improvement of the precision of lattice QCD calculations for the hadronic contributions (contributions of subatomic particles made up of quarks held together by the strong nuclear force) could explain if the disagreement between the prediction and the measured value is due to unknown effects within the QCD or if it is a contribution of new physics beyond the Standard Model [11].

2.7 The 2-Higgs-Doublet Model

The 2HDM is an extension of the existing Standard Model. It is a theory that could explain the deviation in the anomalous magnetic moment of the muon. This theory adds four additional Higgs bosons, to the already existing one. Two neutral Higgs bosons with h being lighter than H (one of the these two bosons is the already discovered Higgs boson with a mass of $m_{\mathrm{higgs}} = 125$ GeV), two CP-even charged Higgs bosons H^+ and H^- and the CP-odd neutral A boson are being predicted [21].
If one of the four bosons is found, it is very likely that the other three also exist. This thesis is based on the search for the A boson.

3 Experimental Setup

3.1 The LHC

The large hadron collider (LHC) is the largest particle accelerator in the world, located at the "Conseil Européen pour la Recherche Nucléaire" (CERN). It is a cyclic accelerator, which makes it possible to accelerate particles, on a length of 26.7 km, up to a collision energy of 13.6 TeV. To bring the particles to this energy they are sped up prior by different small accelerators. Then the protons or heavy led ions inside the LHC are accelerated in two different direction and brought to collision in one of the four detectors. Moved by a strong magnetic field which is produced by superconducting electromagnets the particles travel with nearly the speed of light in ultra-high vacuum. The electromagnets operate in a state of superconductivity which means that the magnets are cooled down to -271.3 °C. To keep the particles on a circular path the LHC uses 1232 dipole magnets. To focus the beam before the collisions there are 392 quadrupole magnets in use. Every 25 ns two packets with 10^{11} protons each collide with one another [10]. This leads to a high luminosity L, which is a measure of particle collisions per area and time. A high luminosity is especially important to have a high number of events to find rare processes. The following relation can be established for the number of events per second N_{events} with the cross-section σ_{event}:

$$N_{\text{events}} = L_{\text{event}}$$

The cross-section indicates the probability of a specific process that takes place during particle interactions.
There are four major experiments installed around the LHC. Apart from the ATLAS experiment, which will be discussed further in this thesis, the CMS, LHCb and ALICE experiments are in use. ATLAS and CMS are designed to make a wide range of different analyses possible. They have the same scientific goals, but use different magnet system designs and different technical approaches. The LHCb is specialised to work with the bottom quark to research the slight differences between matter and anti-matter, while ALICE is used to study heavy-ion physics [10].

3.2 ATLAS

The ATLAS detector (A Toirodal LHC ApparatuS) is build like a cylinder around the particle beam (Figure 3.1). It has a length of 46 m and a height of 25 m with the collision point being located right in the center of the detector. It is able to observe up to 1.7 million collisions per second, which corresponds to a data volume of around 60 megabytes per second. Since the amount of data that is produced at the ATLAS detector is to large to save, a trigger system is used. It filters all of the events for interesting characteristics.
Since many physically interesting particles decay before they are able to be measured, only the final states are detected. It is not possible to detect neutrinos with the ATLAS

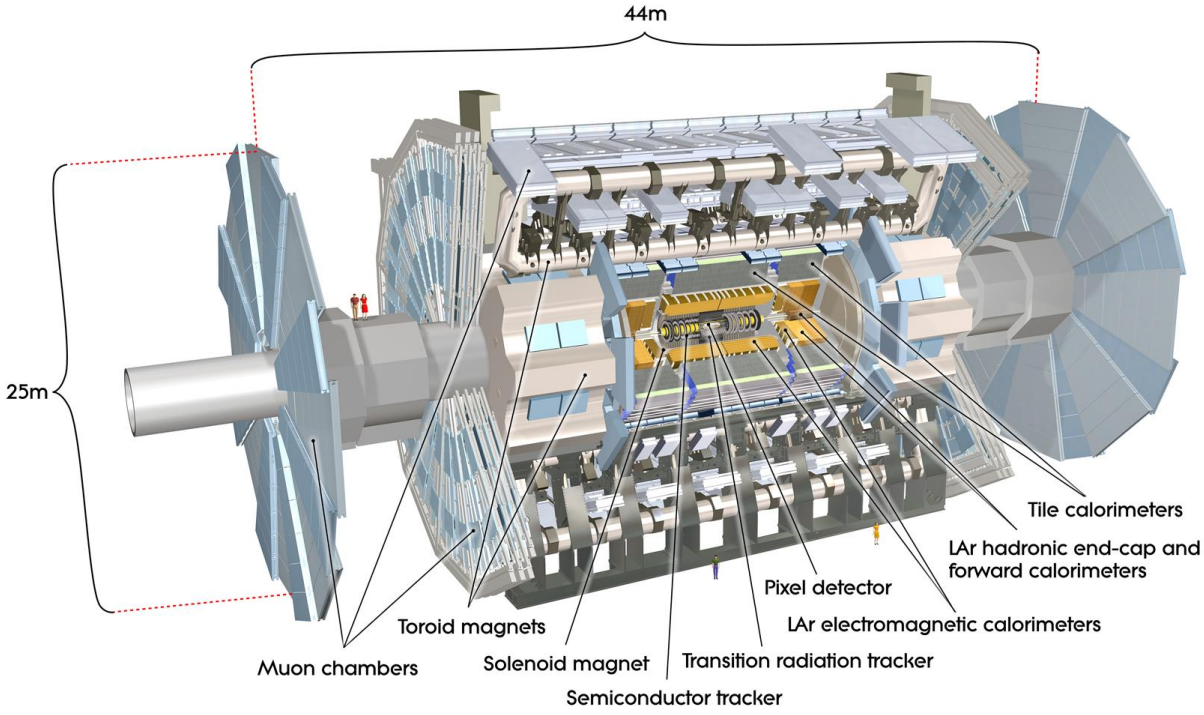

Figure 3.1: A cutaway view of the entire ATLAS detector [1].

detector, because they rarely interact with matter. However following the conservation of moment, the sum of all momenta perpendicular to the X-axis must be zero. This means that the missing transverse momentum $E_{\mathrm{T}}^{\mathrm{miss}}$ can be calculated and be associated with neutrinos or other weakly interacting particles [15].

The Inner Detector

The Inner Detector consists of the Pixel Detector, the Semi Conductor Tracker and the Transition Radiation Tracker. Here, the particle tracks are deflected from their path according to their momentum and charge. Since the magnetic field is known, the momentum of the particles is reconstructed, so particle tracks of electrically charged particles can be identified [15].

The Calorimeter

The calorimeter consists of two primary components, the Liquid Argon Calorimeters (LAr) and the Hadronic Tile Calorimeters. Together they measure the energy of photons, electrons and hadrons. In the LAr, in regular intervals copper plates, which serve as an absorber and liquid argon, which serves as an emitter, are arranged. If a particle hits the absorber, it is being converted into a particle shower. Those daughter particles ionize the liquid argon, which sets free electrons, which then can be measured as electric current. The combined current of all the daughter particles corresponds to the energy of the original particle.

The Hadronic Tile Calorimeters are located around the LAr and detect all of the hadronic particles, which were not absorbed in the LAr. It works after the same principle as the LAr, but with layers of steel and plastic scintillating tiles. Most particles, that are detected in the calorimeters, are leaving all of their energy in this layer of the ATLAS detector [15].

The Muon Spectrometer

Only muons and neutrinos are able to reach this layer of the detector. Since the neutrinos do not interact with the detector only the muons are being detected. Most of the particles either lose their energy or are absorbed by the dense layers of material in the inner parts of the detector through electromagnetic or strong interactions. In contrast, muons do not interact via the strong force and carry a relatively high mass which allows them to go through the detector layers with minimal energy loss. Like in the Inner Detector the track curved by a magnetic field is being measured [15].

3.3 The ATLAS coordinate system

The ATLAS coordinate system is a right-handed coordinate system with its origin being the collision point in the center. The X-axis points towards the center of the LHC tunnel, the Y-axis points upwards and the Z-axis points along the beam axis. The X-Y-plane is called the transverse plane, since it lays orthogonal to the beam.
A point or a location of a particle is described with spherical coordinates. The position is specified by r, θ and ϕ. The radius r is being defined as $r = \sqrt{x^2 + y^2 + z^2}$. The azimuth angle ϕ is being measured in the transverse plane from the X-axis and the angle θ between X and Z-axis. But in the experiment, θ is being measured as pseudorapidity η:

$$\eta = -\ln(\tan(\tfrac{\theta}{2}))$$

This means that a particle which moves parallel to the beam has a pseudorapidity of $\pm\infty$ and one moving away vertically from the Z-axis has one of 0. From this follows, that the angle difference ΔR between two particles can be calculated as [12] :

$$\Delta R = \sqrt{\Delta\eta^2 + \Delta\phi^2}$$

4 Data, Statistics and Methods

4.1 Monte Carlo Simulation

In addition to the data produced in a particle accelerator, simulations are essential for data analyses in particle physics. One method used to simulate the signal and background processes is the Monte Carlo (MC) method. The MC simulations use a theoretical framework, which describes the particle collisions and decays. The simulated events are based on the random sampling from probability distributions, that represent the likelihood of various outcomes [32]. For this analysis data generated with MC has been used for all background and signal events, except for the 'fake' lepton background which was estimated from data [14].

4.2 Statistical Methods

In the search for a new particle, it is in most cases not possible to detect the particle itself. Most particles of interest are not in a stable state and decay before being detected. Instead of looking for an unstable particle, a specific decay channel is considered and the search is carried out by looking for the particle's final states. One of the final states of the CP-odd A boson consists of $e^+\mu^-$ or μ^+e^-. Apart from the reconstructed A boson signal, the background processes must be taken into account. The background consists of muons and electrons that do not result from an A boson decay. Therefore statistical methods are needed to confirm or deny the existence of the boson.
At first, a hypothesis, called the null-hypothesis H_0, is created which corresponds to the SM predictions of the background. Then a second hypothesis H_1 is tested against it. The H_1 consists of the background processes and of the signal process. The data is compared with the two hypotheses. If the data is inconsistent with H_0, but consistent with H_1, then it means that a signal has been observed, which corresponds to the predictions made for H_1. On the other hand, if the data is still compatible with the H_0, then it means that the H_0 cannot be be ruled out with the necessary statistical significances.

4.3 Limit Setting

The maximum value of a parameter which is still statistically compatible with a specific confidence level, is called exclusion. The calculation of exclusion limits is based on profile likelihood-ratio tests. Profile likelihood-ratio tests are powerful statistical methods to compare different hypotheses based on observed values. As mentioned above, the two hypotheses compared in this analysis, are the already introduced H_0 (only background processes) and H_1 (signal and background processes). The parameter μ is introduced to represent the expected signal strength. It is used to scale the expected contribution of a signal. The value of $\mu = 0$ is equivalent to H_0, while $\mu = 1$ is equivalent to H_1

hypothesis [19] [26].
Exclusion limits, also known as upper limits, set a threshold on how large the signal can be relative to the predicted signal strength without being detected. The p_0-value gives an indication of how likely it is that the observed data is occurring under H_0. The smaller the p_0-value the stronger is the evidence against the null hypothesis. To evaluate this, often a p-value threshold of 0.05 is used, meaning H_0 is rejected if $p < 0.05$ [4].

4.4 Applying Cuts

To be able to detect a new particle the signal-to-background ratio is of importance. More precisely the significance Z, which is a quantity that expresses with which certainty a null hypothesis can be excluded, should be as high as possible. This means that a higher Z value indicates a larger separation between the observed signal and the expected background, which suggests that the signal is more statistically significant [6]. The significance can be approximated with the number of background events b and the number of signal events s as follows:

$$Z \approx \frac{s}{\sqrt{b}}$$

The square root of b represents the uncertainty in the background estimation. To get a high significance the ratio between the number of total events and the number of background events must be well balanced. This balance can be achieved by applying certain cuts (selection criteria) on the different parameters of the data set. If for example, the cut $E_{\mathrm{T}}^{\mathrm{miss}} < 50$ GeV is set, all the events with a missing transverse energy greater than 50 GeV, both from the background processes as well as from the signal process, are not being taken into account. If there are more background events being cut than signal events, then the significance improves [20].

4.5 Invariant Mass Reconstruction Methods

Especially in the search for Higgs bosons or Z bosons, invariant mass reconstruction is used to determine the invariant mass of the initially decaying particle. For all decays in which only visible particles are involved, the mass of the original particles can be calculated directly.
On the other hand, the important decay channel for this analysis, is the A boson decay into a τ lepton pair. Each of those τ-leptons then decays involving neutrinos. As stated previously, the detectors are not able to detect the neutrinos. As a result, the energy and momentum taken away by neutrinos cannot be fully measured, they can only be reconstructed.

Collinear Mass Approximation

The collinear mass approximation (COLL) is based on the assumption that in τ-decays the neutrinos and the decay products that can be measured in the detector are collinear and that the mass of the τ-leptons is negligible compared to the mass of the A boson. In this case, collinear means that the particles move in the same directions, therefore their momentum vectors are aligned. The second assumption is that only neutrinos contribute to the missing transverse energy. With those two assumptions the invisible momentum that the neutrinos carry away can be estimated. The invariant mass of the $\tau\tau$-decay $m_{\tau\tau}$ can then be calculated as follows [23]:

$$m_{\tau\tau} = \frac{m_{\text{vis}}}{\sqrt{x_1 x_2}}.$$

The visible mass is thereby m_{vis} and $x_{1;2}$ are the momentum fractions that where carried away by visible decay products. The momentum fractions are calculated with the momentum of the leading lepton p_{leadlep} (lepton with the highest transverse momentum in the event), the momentum of the subleading lepton $p_{\text{subleadlep}}$ (lepton with the second highest transverse momentum in the event) and the missing transverse energy $E^{\text{T}}_{\text{miss}}$ as follows [23]:

$$x_1 = \frac{p_{\text{T}_{\text{leadlep}}}}{p_{\text{T}_{\text{leadlep}}} + E^{\text{T}}_{\text{miss}}},\ x_2 = \frac{p_{\text{T}_{\text{subleadlep}}}}{p_{\text{T}_{\text{subleadlep}}} + E^{\text{T}}_{\text{miss}}}.$$

This method provides a fully reconstructed $\tau\tau$ mass instead of providing only the visible mass, but still has large shortcomings. One example is that this method tends to overestimate the mass of the $\tau\tau$-pairs. Furthermore this method can not give reliable resolutions for events that are back-to-back in the transverse plane of the beam line. If two particles are back-to-back it means that they are emitted in opposite directions relative to each other [23]. This general disadvantage does not effect this analysis, because only collinear processes are looked at.

Missing Mass Calculator

The Missing Mass Calculator (MMC) technique delivers an improved reconstruction of the invariant mass and neutrino mass resolution in $\tau\tau$ final states in comparison to the collinear mass approximation. The MMC takes the kinematic constraints of the decay with its variations of energy and momentum into account. This method assumes that the missing transverse energy is only caused by neutrinos. Each of the events is searched for possible configurations of its visible and invisible τ-decay states. This is done by looking for the most probable values for the unknown variables [23].

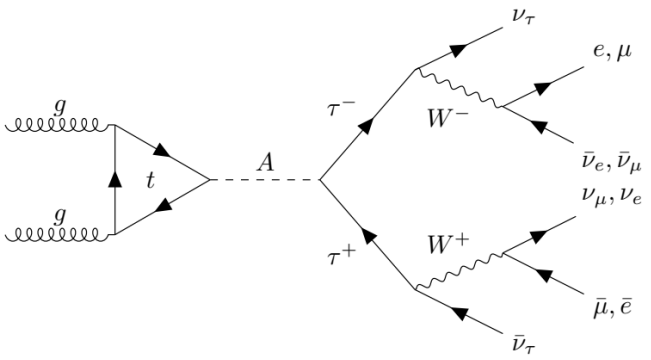

Figure 5.1: Feynman diagram of the full $A \to \tau_{\text{lep}}\tau_{\text{lep}}$ signal process [31].

5 Analysis

5.1 Signal Process

In this thesis the investigated signal process is the decay of the low-mass CP-odd A boson in the range from 20 GeV to 80 GeV. The boson is produced through gluon fusion via a top quark loop. This means, that two gluons interacting with each other can produce an A boson. The gluons cannot interact directly with the A boson because they have a colour charge and are mass-less. However, they can interact indirectly via "loops" of other particles that couple both to gluons and the A boson. Considering the mass of the boson and its possible couplings, the A boson decays almost exclusively into $\tau-$leptons. This $\tau-$leptonpair can decay further into hadrons and leptons. This analysis is focused on the leptonic decays. Because the trigger thresholds are lower than for a hadronic decay, which means, events with lower energy and momentum can now pass the trigger system, in total more events are taken into account. Furthermore they leave a cleaner detector signature. This decay and the production of the A boson can be seen in the Feynman diagram shown in Figure 5.1 [14] [31].

5.2 Background Processes

Apart from the described signal process, many different SM processes are able to produce similar detector signatures. Those processes are producing the background events, which have to be modeled and cut to achieve a high significance. To do this, it is important to identify those different SM processes [14].

$Z^{\gamma^*} \to ll$ Background

The Z boson with a mass of $m_Z \approx 90$ GeV produces a very prominent background, because it shares properties with the A boson. They are both not electrically charged and for a heavy A boson mass hypothesis the mass could almost be identical. Within the $Z \to ll$ decay channel the Z boson decays into an electron positron pair or a muon-antimuon pair. To eliminate this prominent background process, only the decays into a muon and

an electron with their corresponding neutrinos are considered. Because this specific decay does not produce neutrinos, the missing transverse energy $E_{\mathrm{T}}^{\mathrm{miss}}$ is lower in comparison to the signal process.
Apart from the Z boson, off-shell photons can produce background events. Off-shell photons do not satisfy the energy-momentum relation for 'real' photons, which is: $E = p$, with E being the energy of the photon and p being the moment. These processes also contribute to the background because the off-shell photons can also decay into an electron positron pair or a muon-antimuon pair. This background is also cut with the criteria, that only takes events with muon electron pairs into account [14] [28].

$Z^{\gamma^*} \rightarrow \tau\tau$ Background

The $Z^{\gamma^*} \rightarrow \tau\tau$ decay process is the main background of this analysis. It has the same final state as the signal process. Coming from the Z boson or involving off-shell photons, the $\tau-$leptonpairs decay into electrons and muons, which makes it difficult to separate this decay from an A boson decay. Furthermore a possible similar mass of the A and Z boson results in it being only difficultly identifiable over the reconstruction of the mass. In order to separate the final states, the different CP-values and spin are used. They lead to different decay angles between the leptons, which can be measured [14] [28].

Top quark processes

During decays, top quarks can be produced as a pair of top and anti-top quark or individually. Those top quarks then decay with a high probability of 91.4% into a W boson and a bottom quark. The W boson then either decays into a lepton with its corresponding neutrinos or a quark pair. When the top-quarks are produced as a pair and then decay leptonically, then this decay has a similar final state as the signal process. However this process can still be distinguished by its missing transverse energy $E_{\mathrm{T}}^{\mathrm{miss}}$, because it produces less neutrinos than the signal process and therefore a smaller $E_{\mathrm{T}}^{\mathrm{miss}}$. Furthermore the bottom quark can produce a jet, which can be identified as a lepton. Those jets, called b-jets, can be differentiated because they are more stable than regular jets. The rejection of the b-jets leads to a large suppression of the top quark background [14] [28].

SM Higgs processes

The already measured SM Higgs boson with a mass of $m_H = 125$ GeV can produce a muon and electron through two different decay channel. The probability that the Higgs boson decays into a τ lepton pair is with 6.27% relatively low. The second important process is $H \rightarrow WW$. When the two W bosons decay into a muon and electron then they can also contribute to the background. This background can be easily separated from the signal process by its mass, because the SM Higgs has a higher mass than the low-mass A boson [14] [28].

Diboson Processes

Diboson processes are decays in which two bosons of the weak force can be found. The combinations WW, WZ and ZZ can occur. If the two W bosons both decay into leptons the same final state as in the signal process can be produced. To distinguish them from each other, mass variables are used. Furthermore there can be false identifications in the detector, which can produce background events. Still a lot of diboson processes have a final state that differs significantly from the final state of the signal process [14] [28].

Fake Lepton Background

In the ATLAS detector prompt leptons (directly produced in the interaction) can be easily identified, but it is difficult to identify fake leptons (also called non-prompt leptons). These fake leptons often come from decays with jets, particle misidentifications, or interactions with the detector material. It is difficult to model these background processes accurately with simulations. Because the A boson decays into leptons, the fakes also make up a significant amount of the background [28].

5.3 Signal Regions

This analyses is divided into two signal regions (SR): the low-mass signal region for mass hypotheses between 20 GeV and 80 GeV, which this thesis is focused on, and the high mass signal region from 80 GeV to 110 GeV. The signal region is defined differently because the intensity of certain backgrounds differ depending on the mass hypothesis as well as some of the parameters of the decay. One prominent example is the Z background, since $m_Z = 90$ GeV, it is relevant in the high mass SR and accordingly not as relevant in the low mass SR. This means that cuts can be set accurately for each signal region. This leads to a better combined significance and therefore upper limit [14].

5.4 Uncertainties

In this analysis different systematic and statistical uncertainties occurred. Systematic uncertainties are the most significant and can be divided into experimental and theoretical uncertainties. The experimental uncertainties mostly arise from measurements and detector simulations. They are process-independent but affect the reconstruction of particles (e.g., leptons and jets) [7]. The theoretical uncertainties on the other hand are specific to the particle interactions and the modeling processes, such as uncertainties in cross-sections for various particle interactions, like $Z \to \tau\tau$ processes or top-quark processes [30]. In addition, statistical uncertainties occur, which can be described by the Poisson distribution. The systematic uncertainties are not taken into account in this thesis.

6 Cut Optimization

To maximize the significance of the signal, a cut optimization is done by looking at different distributions of variables and setting cuts to remove the bins (intervals or divisions that group data points into ranges), in which the background events are more prominent than the signal events. From the significance, which is calculated as: $Z = \frac{s}{\sqrt{b}}$ (as explained in chapter 4.4), also follows that a smaller number of total events lead to a deterioration of the significance. During a cut optimization the optimal ratio between cutting the background and keeping most of the signal events must be found.
To see the difference before and after a cut, limit plots are used. They show, for each A boson mass from 20 GeV to 80 GeV, the needed signal strength μ so that the p_0-value is less than 0.05. The signal strength is indicated as the $gg \to A$ production cross-section (measure of the probability for an A boson to occur in a particle collision) times the branching ratio for an A boson decay into two τ-leptons (probability that an A boson decay will result in a τ-lepton further decaying into a μe, $\mu\mu$ or ee final state, compared to all possible decay modes):

$$\sigma(gg \to A) \times B(A \to \tau_{\text{lep}}\tau_{\text{lep}})$$

A higher significance therefore leads to a smaller necessary μ to qualify for $p_0 < 0.05$, meaning that a lower $\sigma(gg \to A) \times B(A \to \tau_{\text{lep}}\tau_{\text{lep}})$ is sufficient to be certain that the observed data is not occurring under H_0, if the significance is higher.
The upper limits with the different implemented cuts (baseline cuts and additional cuts) are compared to the upper limit with no additional cuts (baseline cuts). This means that only the baseline cuts have been implemented in the "no cut" references. The baseline selection states, that each event must contain one electron ($p_{\text{T}}^e > 18$ GeV) and one muon ($p_{\text{T}}^\mu > 15$ GeV). Additionally the electric charge of the two leptons must meet the following criterion: $q_e \cdot q_\mu = -1$. The particles also have to be measured in certain detector regions ($|\eta_e| < 2.47$ excluding $1.37 < |\eta_e| < 1.52$ and $|\eta_\mu| < 2.7$). Finally, only events without b-jets and a jet transverse momentum over 20 GeV are being taken into account [28]. This cut optimization was done for the low-mass signal region (LMSR).

6.1 Cuts on MMC Variables

In this section the cuts which maximize the significance of the signal of the A boson and therefore optimize the upper limit, while using the MMC method, are being introduced.

Missing Transverse Energy Cut

The missing transverse energy, denoted as $E_{\text{T}}^{\text{miss}}$, represents the energy that cannot be directly detected in the experiment but is required by the principles of energy and momentum conservation. Responsible for the $E_{\text{T}}^{\text{miss}}$ are the neutrinos, which do not interact with the detector and therefore remain invisible [25]. This is further explained in

chapter 3.2 “ATLAS”. In Figure 6.1a a distribution of the number of events measured for their corresponding $E_{\mathrm{T}}^{\mathrm{miss}}$ is shown. In the range between 0 GeV and 60 GeV, the background events are way more prominent than the signal events, so the cut $E_{\mathrm{T}}^{\mathrm{miss}} > 60$ GeV is set (Figure 6.1b). This cut follows from the top quark processes, because they produce a smaller $E_{\mathrm{T}}^{\mathrm{miss}}$, than the signal process and therefore more background events in the lower mass ranges. This is further explained in chapter 5.2 “Background Processes”. Also more ‘fakes’ are being measured in this range, compared to higher $E_{\mathrm{T}}^{\mathrm{miss}}$ events.
This is why this cut leads to an improvement of the upper limit in comparison to the upper limit without any additional cuts, in the range from 20 GeV to around 60 GeV, as can be seen in the limit plot with its corresponding ratio plot (Figure 6.2). The highest improvement with around 45%, can be seen between 30 GeV and 40 GeV. On the other hand a deterioration can be seen in the higher mass ranges from around 60 GeV to 80 GeV, because a lot of signal events in this higher mass ranges have been cut. In comparison to an $E_{\mathrm{T}}^{\mathrm{miss}} > 50$ GeV cut or $E_{\mathrm{T}}^{\mathrm{miss}} > 70$ GeV cut, the $E_{\mathrm{T}}^{\mathrm{miss}} > 60$ GeV cut shows the highest improvement. If the variable is cut with the $E_{\mathrm{T}}^{\mathrm{miss}} > 50$ GeV cut, the limit deteriorates in comparison up to 15% . On the other hand if the cut is set with $E_{\mathrm{T}}^{\mathrm{miss}} > 70$ GeV the limit only deteriorates in the lower mass ranges up to 15% and improves at around 50 GeV up to 7%. The limit plots for the comparison cuts are shown in the Appendix A.1.

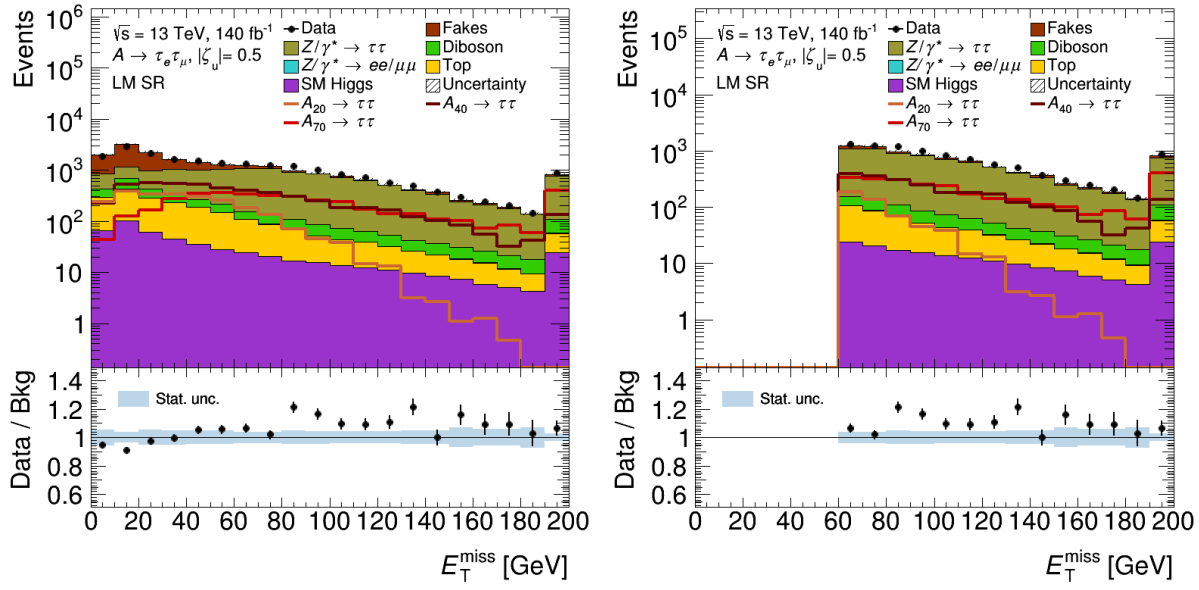

(a) (b)

Figure 6.1: Distribution of the $E_{\mathrm{T}}^{\mathrm{miss}}$ variable without (6.1a) and with (6.1b) the $E_{\mathrm{T}}^{\mathrm{miss}} > 60$ GeV cut, shown from 0 GeV to 200 GeV in bins of 10 GeV. The various colors in the stacked histograms show contributions from various background processes and the $A \to \tau\tau$ signal are presented as lines in shades of red for different mass hypotheses. The last bin is used as an overflow bin (all access events which where measured outside the range of the scale of the x-axis, are being combined in this bin). The scale used for the number of events in the plots is logarithmic. The blue band in the ratio plot shows the uncertainties from statistical sources.

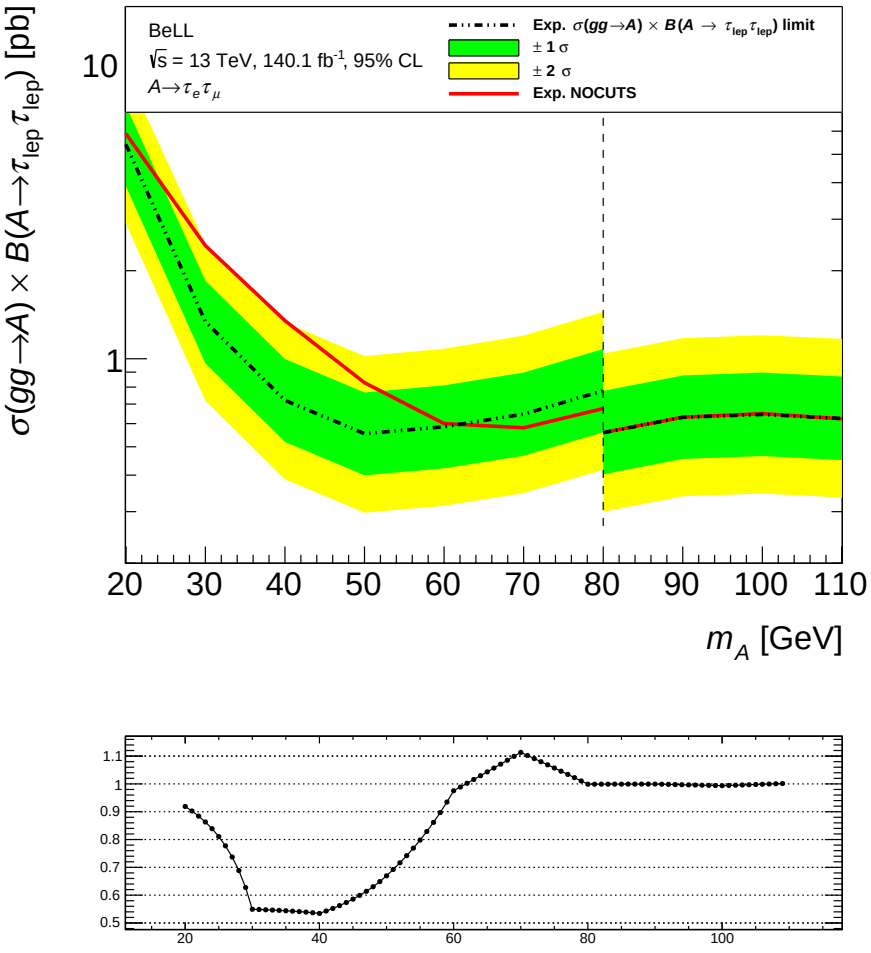

Figure 6.2: Upper limits with and without the $E_{\mathrm{T}}^{\mathrm{miss}} > 60$ GeV cut on the $gg \to A$ production cross-section times the branching ratio for an A boson decay into two τ-leptons, which further decay into a μe, $\mu\mu$ or ee final state, for A boson masses from 20 to 80 GeV. The dash-dotted line shows limit with the cut and with its 1σ and 2σ uncertainty bands in green and yellow. The solid red line shows the limit without any additionally implemented cuts (reference). The vertical dashed line indicates the splitting of the SR: only the low-mass hypotheses on the left side are being cut optimized in this work. The ratio plot beneath the limit plot shows the improvement or the deterioration of the limit (dashed line) in comparison to the reference (red line). The y-axis is plotted as: ratio $= \frac{\text{limit}}{\text{reference}}$, with $y = 1$ being the perfect agreement between the limit with the additional cut and the reference. The deviations of 1 indicate whether the limit has improved ($y < 1$) or deteriorated ($y > 1$) in comparison to the reference limit.

Higgs Transverse Momentum Cut

The transverse momentum of the Higgs $p_{\mathrm{T}}^{\mathrm{higgs}}$ describes the momentum of the A boson perpendicular to the beam axis. In the lower $p_{\mathrm{T}}^{\mathrm{higgs}}$ ranges, again a lot of fake background was measured, which can be seen in Figure 6.3a. Furthermore the signal for the different A boson masses are not as strong in the lower mass ranges from 0 GeV to around 110 GeV as in the higher mass ranges. This is because, a property of the A boson is large $p_{\mathrm{T}}^{\mathrm{higgs}}$ [14], which leads to the $p_{\mathrm{T}}^{\mathrm{higgs}} > 110$ GeV cut being set. The cut is visualized in Figure 6.3b.

This cut leads to an improvement in the mass range from 20 GeV to approximately 65 GeV with up to 50% in comparison to the upper limit without any additional cuts (Figure 6.4). In the higher mass ranges again a deterioration is noticeable of up to 4%. If the cut is set lower such as $p_{\mathrm{T}}^{\mathrm{higgs}} > 100$ GeV the limit deteriorates slightly up to 4.5% between 30 GeV and 70 GeV. In the lower ranges between 20 GeV and 30 GeV however an improvement of up to 4% can be seen. Since this effects a much smaller mass range the $p_{\mathrm{T}}^{\mathrm{higgs}} > 110$ GeV cut is kept. If the cut is set higher at $p_{\mathrm{T}}^{\mathrm{higgs}} > 120$ GeV the limit deteriorates up to 20%, especially in the lower ranges compared to the $p_{\mathrm{T}}^{\mathrm{higgs}} > 110$ GeV cut. An slight improvement with up to 7% can be seen in the higher mass ranges. The limit plots for the comparison cuts are shown in the Appendix A.2.

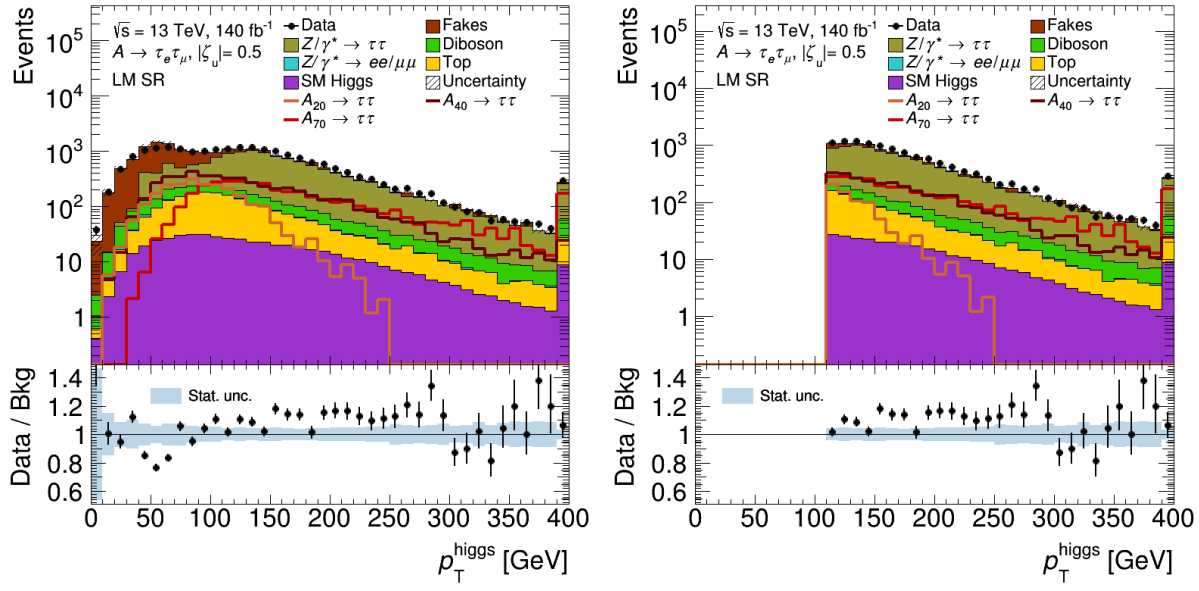

(a) (b)

Figure 6.3: Distribution of the $p_{\mathrm{T}}^{\mathrm{higgs}}$ variable without (6.3a) and with (6.3b) the $p_{\mathrm{T}}^{\mathrm{higgs}} > 110$ GeV cut, shown between 0 GeV and 400 GeV in bins of 10 GeV. The various colors in the stacked histograms show contributions from various background processes and the $A \to \tau\tau$ signal are presented as lines in shades of red for different mass hypotheses. The last bin is used as an overflow bin. The scale used for the number of events in the plots is logarithmic. The blue band in the ratio plot shows the uncertainties from statistical sources.

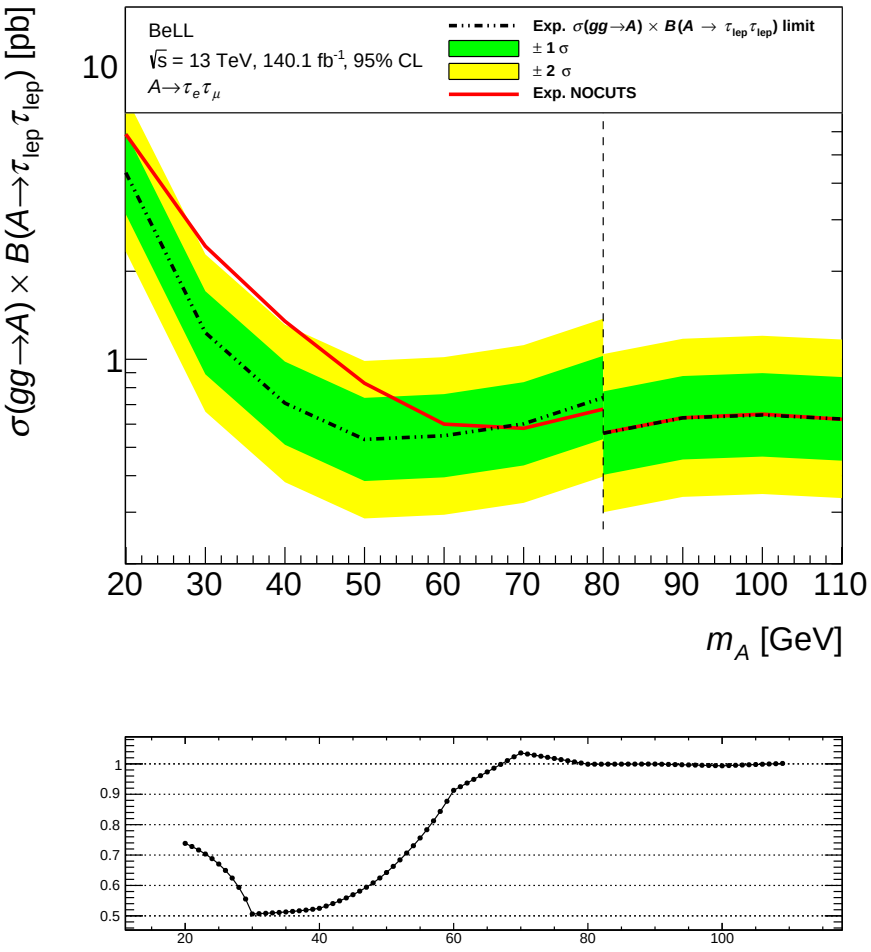

Figure 6.4: Upper limits with and without the $p_{\mathrm{T}}^{\mathrm{higgs}} > 110$ GeV cut on the $gg \to A$ production cross-section times the branching ratio for an A boson decay into two τ-leptons, which further decay into a μe, $\mu\mu$ or ee final state, for A boson masses from 20 to 80 GeV. The dash-dotted line shows limit with the cut and with its 1σ and 2σ uncertainty bands in green and yellow. The solid red line shows the limit without any additionally implemented cuts (reference). The vertical dashed line indicates the splitting of the SR: only the low-mass hypotheses on the left side are being cut optimized in this work. The ratio plot beneath the limit plot shows the improvement or the deterioration of the limit (dashed line) in comparison to the reference (red line). The y-axis is plotted as: ratio $= \frac{\text{limit}}{\text{reference}}$, with $y = 1$ being the perfect agreement between the limit with the additional cut and the reference. The deviations of 1 indicate whether the limit has improved ($y < 1$) or deteriorated ($y > 1$) in comparison to the reference limit.

Jet Transverse Momentum Cut

The jet transverse momentum $p_{\mathrm{T}}^{\mathrm{jet}}$ refers to the momentum of a jet in the plane perpendicular to the beam axis. It is calculated by summing up the values of all particles within the jet. The measured events become less frequent with increasing $p_{\mathrm{T}}^{\mathrm{jet}}$. Since it is a logarithmic scale, there are more background events than signal events in the lower mass ranges, as can be seen in Figure 6.5a. Because the A boson has a high p_{T}, the jets also need to have a high p_T because of the law of conservation of momentum. Since momentum is conserved in all directions, this means that the vector sum of the momenta of the decay products have to be equal the momentum of the original particle before decay [33]. This leads to the cut being set as $p_{\mathrm{T}}^{\mathrm{jet}} > 30$ GeV, as portrayed in Figure 6.5b.
This cut shows an overall optimization of the upper limit in comparison to the upper limit without any additional cuts (Figure 6.6). The improvement is consistent at around 20% to 30% in all mass ranges.
If the cut is set higher at $p_{\mathrm{T}}^{\mathrm{jet}} > 40$ GeV a deterioration of up to 12% occurs in comparison to the $p_{\mathrm{T}}^{\mathrm{jet}} > 40$ GeV cut. Because the cut is already set relatively low, a lower cut is not sensible. The limit plot for the comparison cut is shown in the Appendix A.3.

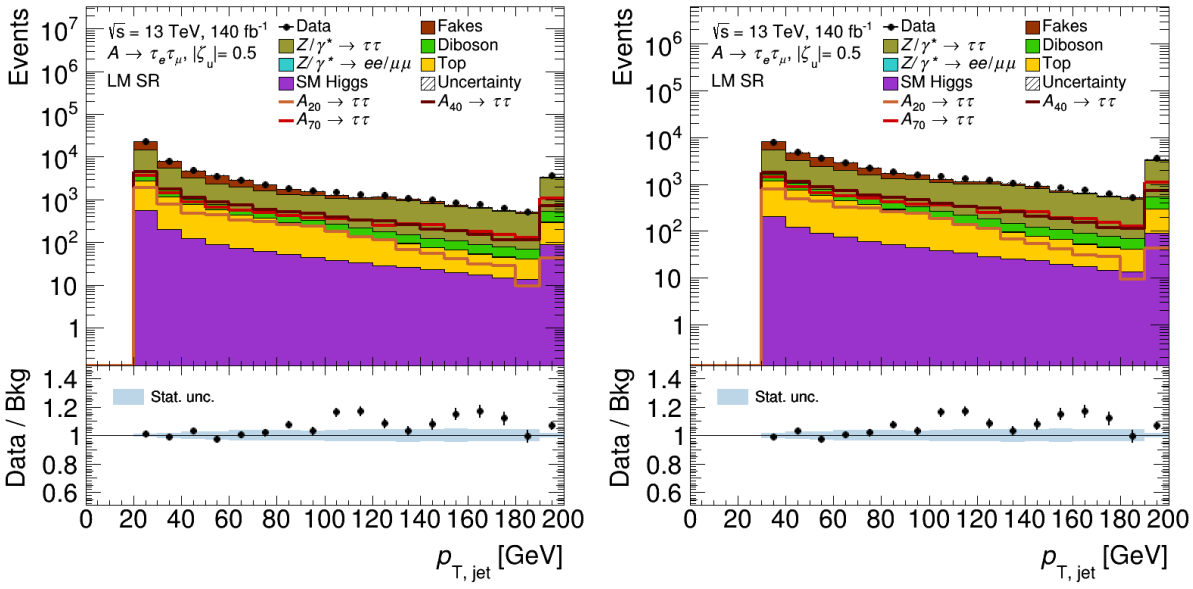

(a) (b)

Figure 6.5: Distribution of the $p_{\mathrm{T}}^{\mathrm{jet}}$ variable without (6.5a) and with (6.5b) the $p_{\mathrm{T}}^{\mathrm{jet}} > 30$ GeV cut, shown between 20 GeV and 200 GeV in bins of 10 GeV. The various colors in the stacked histograms show contributions from various background processes and the $A \to \tau\tau$ signal are presented as lines in shades of red for different mass hypotheses. The last bin is used as an overflow bin. The scale used for the number of events in the plots is logarithmic. The blue band in the ratio plot shows the uncertainties from statistical sources.

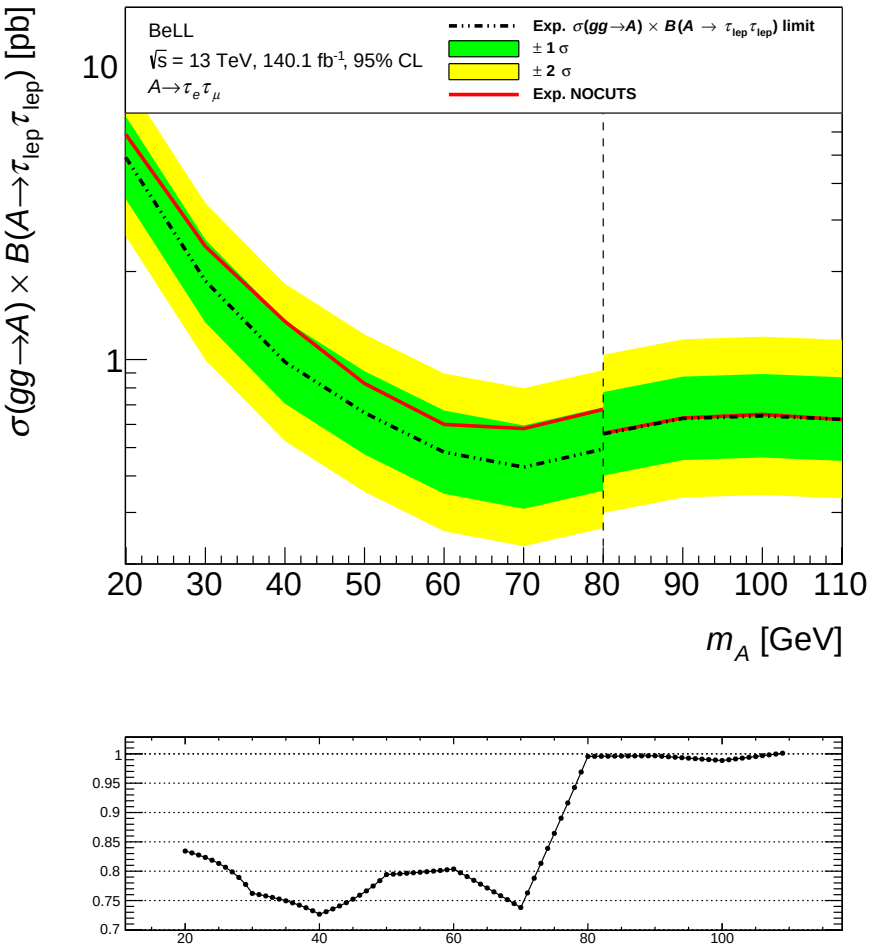

Figure 6.6: Upper limits with and without the $p_{\mathrm{T}}^{\mathrm{jet}} > 30$ GeV cut on the $gg \to A$ production cross-section times the branching ratio for an A boson decay into two τ-leptons, which further decay into a μe, $\mu\mu$ or ee final state for A boson masses from 20 to 80 GeV. The dash-dotted line shows limit with the cut and with its 1σ and 2σ uncertainty bands in green and yellow. The solid red line shows the limit without any additionally implemented cuts (reference). The vertical dashed line indicates the splitting of the SR: only the low-mass hypotheses on the left side are being cut optimized in this work. The ratio plot beneath the limit plot shows the improvement or the deterioration of the limit (dashed line) in comparison to the reference (red line). The y-axis is plotted as: ratio $= \frac{\text{limit}}{\text{reference}}$, with $y = 1$ being the perfect agreement between the limit with the additional cut and the reference. The deviations of 1 indicate whether the limit has improved ($y < 1$) or deteriorated ($y > 1$) in comparison to the reference limit.

$\Delta R_{\text{lep,lep}}$ Cut

The angle distance $\Delta R_{\text{lep,lep}}$ describes the separation between two leptons in the detector and is further described in chapter 2.3 "The ATLAS Coordinate System". The distribution of this variable is shown in Figure 6.7a. It can be seen that the larger the angle, the larger the Z background becomes. In addition, the signal events become less prominent at larger values of the angle, which leads to the $\Delta R_{\text{lep,lep}} < 0.6$ cut being set (Figure 6.7b). This cut significantly reduces the $Z \to \tau\tau$ background, because in comparison to the A boson, the leptons of the $Z \to \tau\tau$ decay produce a larger ΔR angle [14]. This larger angle is caused by the different spin and CP-values as well as the larger mass of the Z boson compared to the A boson.

This cut ensures an improvement in all the mass ranges (Figure 6.8) compared to the limit without any additional cuts. The biggest optimization can be seen at around 40 GeV with 55%. If the cut is set at $\Delta R_{\text{lep,lep}} < 0.4$ the limit deteriorates up to 50% and if the cut is set higher at $\Delta R_{\text{lep,lep}} < 0.8$ the limit deteriorates up to 40% compared to the $\Delta R_{\text{lep,lep}} < 0.6$ cut. The limit plots of the comparison cuts are shown in the Appendix A.4.

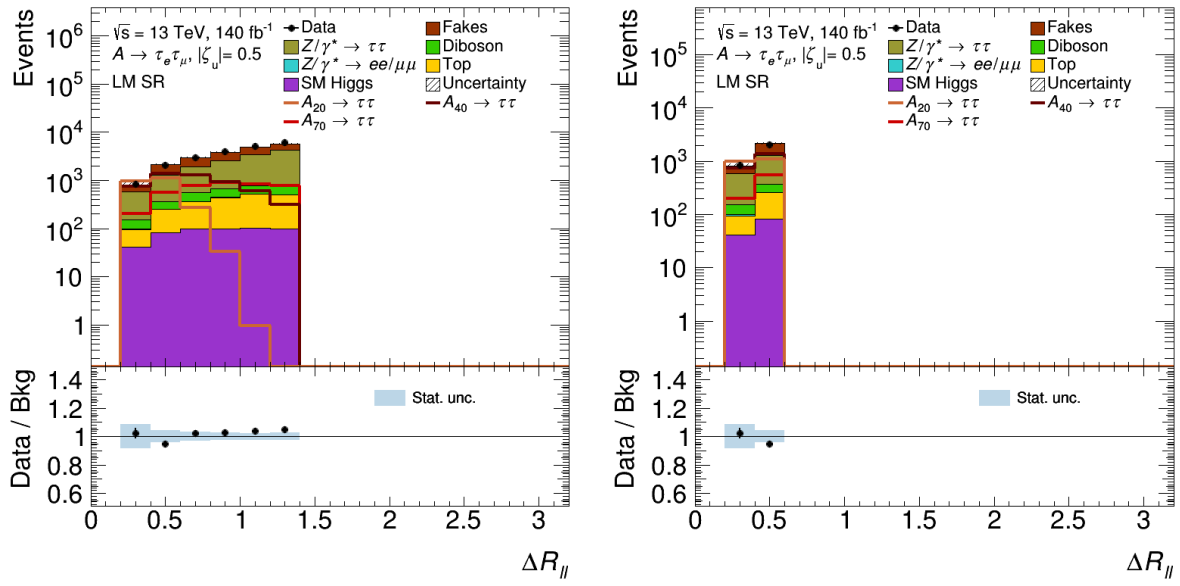

(a) (b)

Figure 6.7: Distribution of the $\Delta R_{\text{lep,lep}}$ variable without (6.7a) and with (6.7b) the $\Delta R_{\text{lep,lep}} < 0.6$ cut, shown between 0.2 and 1.4 in bins of 0.2. This variable has no unit. The various colors in the stacked histograms show contributions from various background processes and the $A \to \tau\tau$ signal are presented as lines in shades of red for different mass hypotheses. The last bin is used as an overflow bin. The scale used for the number of events in the plots is logarithmic.The blue band in the ratio plot shows the uncertainties from statistical sources.

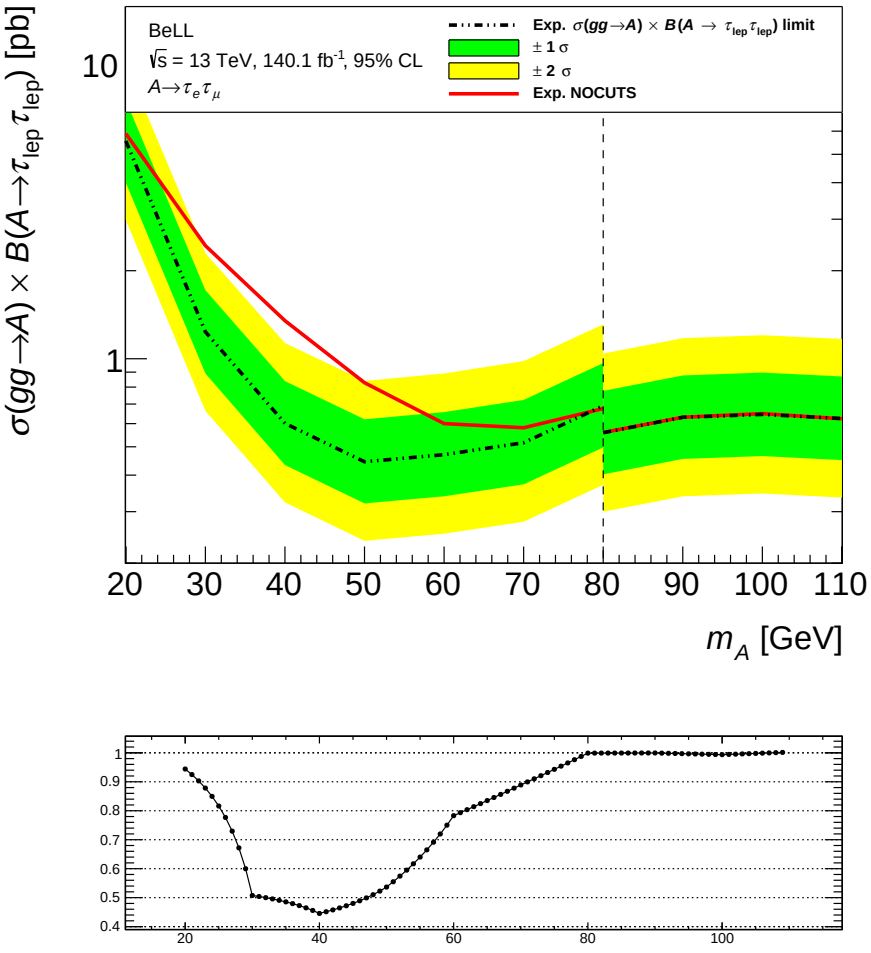

Figure 6.8: Upper limits with and without the $\Delta R_{\text{lep,lep}} < 0.6$ cut on the $gg \to A$ production cross-section times the branching ratio for an A boson decay into two τ-leptons, which further decay into a μe, $\mu\mu$ or ee final state for A boson masses from 20 to 80 GeV. The dash-dotted line shows limit with the cut and with its 1σ and 2σ uncertainty bands in green and yellow. The solid red line shows the limit without any additionally implemented cuts (reference). The vertical dashed line indicates the splitting of the SR: only the low-mass hypotheses on the left side are being cut optimized in this work. The ratio plot beneath the limit plot shows the improvement or the deterioration of the limit (dashed line) in comparison to the reference (red line). The y-axis is plotted as: ratio $= \frac{\text{limit}}{\text{reference}}$, with $y = 1$ being the perfect agreement between the limit with the additional cut and the reference. The deviations of 1 indicate whether the limit has improved ($y < 1$) or deteriorated ($y > 1$) in comparison to the reference limit.

Combined MMC Cuts

In Figure 6.9b, the MMC mass variable m_{MMC} is depicted with all the mentioned cuts which means that all the background and signal events which do not fulfill the criteria of $E_{\text{T}}^{\text{miss}} > 60$ GeV, $p_{\text{T}}^{\text{higgs}} > 110$ GeV, $p_{\text{T}}^{\text{jet}} > 30$ GeV and $\Delta R_{\text{lep,lep}} < 0.6$, are cut. There can be seen an improvement of the background-to-signal ratio in comparison to Figure 6.9a, which shows the m_{MMC} variable without any additional cuts. The limit and ratio plot for all the mentioned cuts combined are depicted in Figure 6.10. In total, a large improvement can be seen. However the largest optimization of the upper limit with around 70% can be found at 40 GeV. The improvements are generally higher in the medium masses of this signal region, because the higher masses are more influenced by the Z boson and this cut optimization was primarily done for ranges with few Z influence. This leads to an improvement of maximum 55% in the range between 60 GeV and 80 GeV. On the other hand, there was only an improvement of around 30% at 20 GeV.

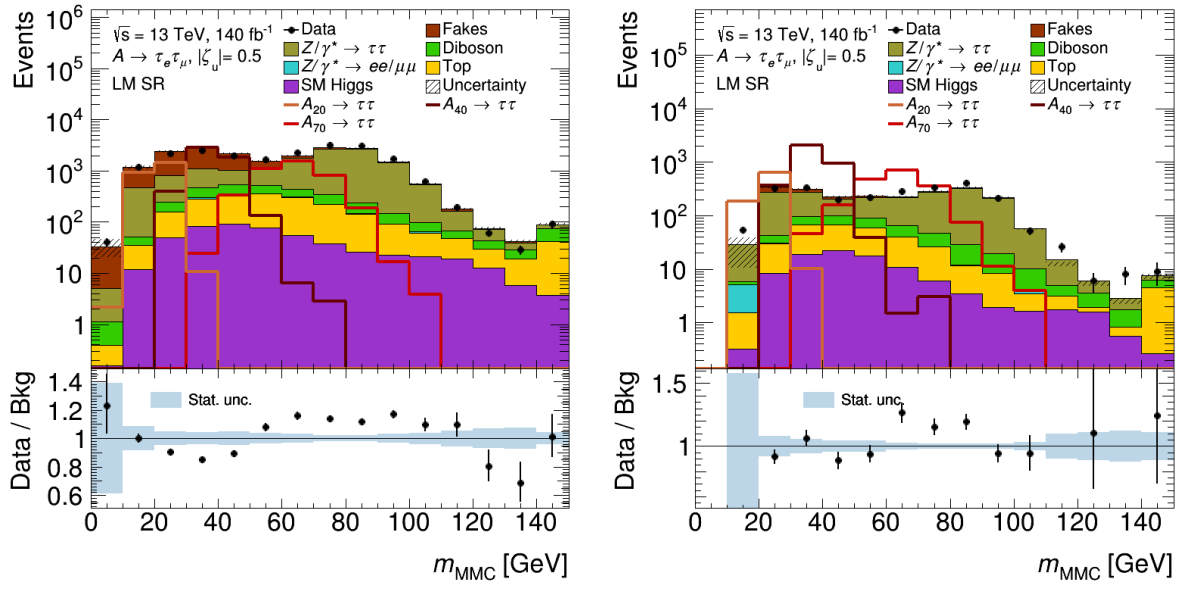

(a) (b)

Figure 6.9: Distribution of the m_{MMC} variable without (a) and with (b) the combined cuts ($E_{\text{T}}^{\text{miss}} > 60$ GeV, $p_{\text{T}}^{\text{higgs}} > 60$ GeV, $p_{\text{T}}^{\text{jet}} > 40$ GeV and $\Delta R_{\text{lep,lep}} < 0.6$), shown between 0 GeV and 150 GeVin bins of 10 GeV. The various colors in the stacked histograms show contributions from various background processes and the $A \to \tau\tau$ signal are presented as lines in shades of red for different mass hypotheses. The scale used for the number of events in the plots is logarithmic. The blue band in the ratio plot shows the uncertainties from statistical sources.

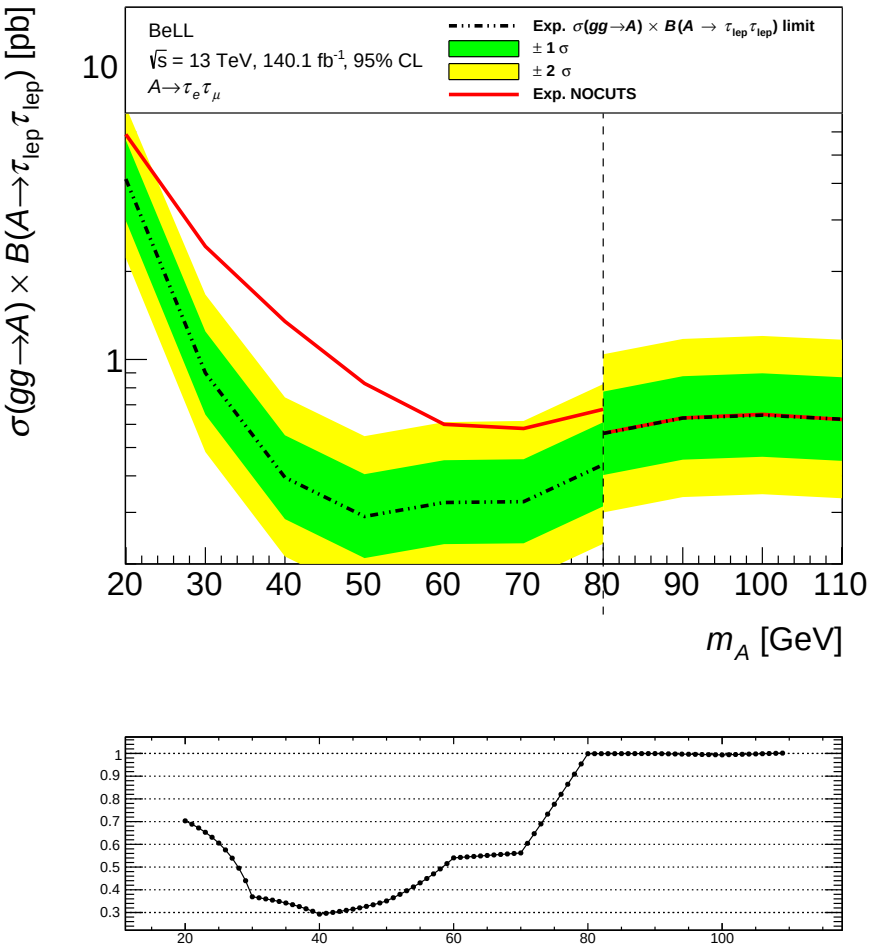

Figure 6.10: Upper limits with and without the combined cuts ($E_{\mathrm{T}}^{\mathrm{miss}} > 50$ GeV, $p_{\mathrm{T}}^{\mathrm{higgs}} > 110$ GeV, $p_{\mathrm{T}}^{\mathrm{jet}} > 30$ GeV and $\Delta R_{\mathrm{lep,lep}} < 0.6$) on the $gg \to A$ production cross-section times the branching ratio for an A boson decay into two τ-leptons, which further decay into a μe, $\mu\mu$ or ee final state for A boson masses from 20 to 80 GeV. The dash-dotted line shows limit with the cuts and with its 1σ and 2σ uncertainty bands in green and yellow. The solid red line shows the limit without any additionally implemented cuts (reference). The vertical dashed line indicates the splitting of the SR: only the low-mass hypotheses on the left side are being cut optimized in this work. The ratio plot beneath the limit plot shows the improvement or the deterioration of the limit (dashed line) in comparison to the reference (red line). The y-axis is plotted as: ratio $= \frac{\text{limit}}{\text{reference}}$, with $y = 1$ being the perfect agreement between the limit with the additional cuts and the reference. The deviations of 1 indicate whether the limit has improved ($y < 1$) or deteriorated ($y > 1$) in comparison to the reference limit.

6.2 Cuts on COLL Variables

In this section the cuts which maximize the significance of the A boson signal and therefore optimize the upper limit, while using the collinear mass approximation, are being introduced. Since the cuts for the COLL reconstruction method are almost identical to the cuts of the MMC mass reconstruction method, the explanations for the cuts, as well as the explanations of their effects can be found in chapter 6.1 "Cuts on MMC Variables".

Missing Transverse Energy Cut

In Figure 6.11a a distribution of the number of events measured for their corresponding $E_{\mathrm{T}}^{\mathrm{miss}}$ are shown. In the range between 0 GeV and 60 GeV, the background events are way more prominent than the signal events (Figure 6.1a), so the cut $E_{\mathrm{T}}^{\mathrm{miss}} > 60$ GeV is set (Figure 6.11b).
This cut leads to an improvement of the upper limit for all mass ranges, compared to the upper limit without any additional cuts, as can be seen in the limit plot with its corresponding ratio plot (Figure 6.12). The highest improvement can be seen at 30 GeV with about 45%. In comparison to an $E_{\mathrm{T}}^{\mathrm{miss}} > 50$ GeV cut or an $E_{\mathrm{T}}^{\mathrm{miss}} > 70$ GeV cut, the $E_{\mathrm{T}}^{\mathrm{miss}} > 60$ GeV cut shows the highest improvement. If the variable is cut with the $E_{\mathrm{T}}^{\mathrm{miss}} > 50$ GeV cut, the limit deteriorates in comparison up to 15%. However, there can also be seen an improvement of up to 14% in the lower mass ranges, but since the deterioration effects a larger mass range, the $E_{\mathrm{T}}^{\mathrm{miss}} > 60$ GeV cut leads to a overall higher improvement. On the other hand if the cut is set as $E_{\mathrm{T}}^{\mathrm{miss}} > 70$ GeV the limit deteriorates in the lower mass ranges up to 27% and improves at around 40 GeV up to 4%. The limit plots for the comparison cuts are shown in the Appendix A.5.

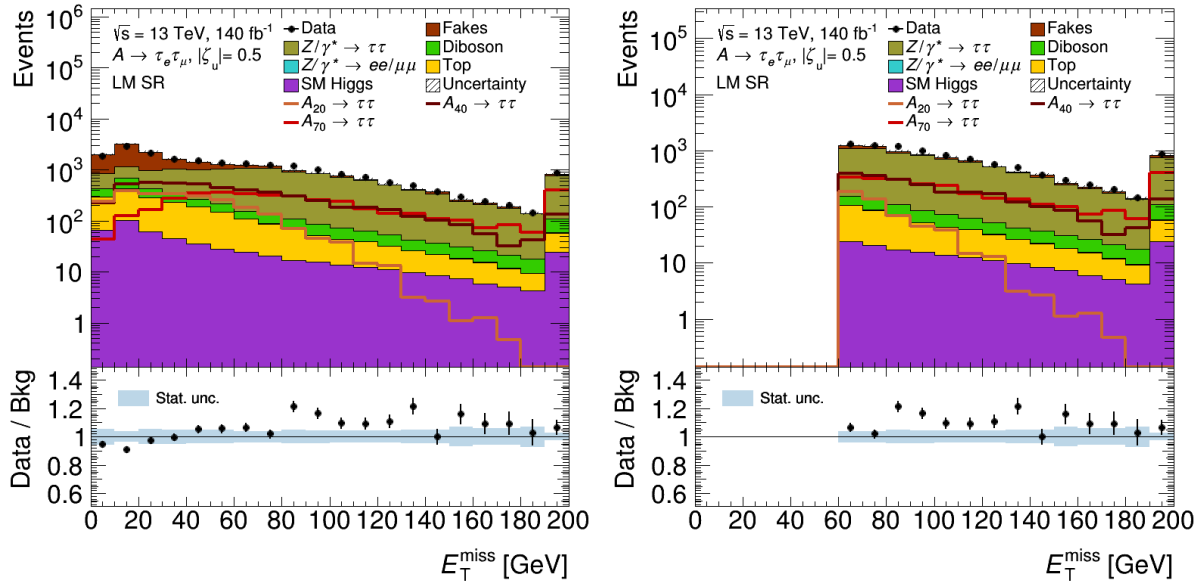

(a) (b)

Figure 6.11: Distribution of the $E_{\mathrm{T}}^{\mathrm{miss}}$ variable without (6.11a) and with (6.11b) the $E_{\mathrm{T}}^{\mathrm{miss}} > 60$ GeV cut, shown from 0 GeV to 200 GeV in bins of 10 GeV. The various colors in the stacked histograms show contributions from various background processes and the $A \to \tau\tau$ signal are presented as lines in shades of red for different mass hypotheses. The last bin is used as an overflow bin (all access events which where measured outside the range of the scale of the x-axis, are being combined in this bin). The scale used for the number of events in the plots is logarithmic. The blue band in the ratio plot shows the uncertainties from statistical sources.

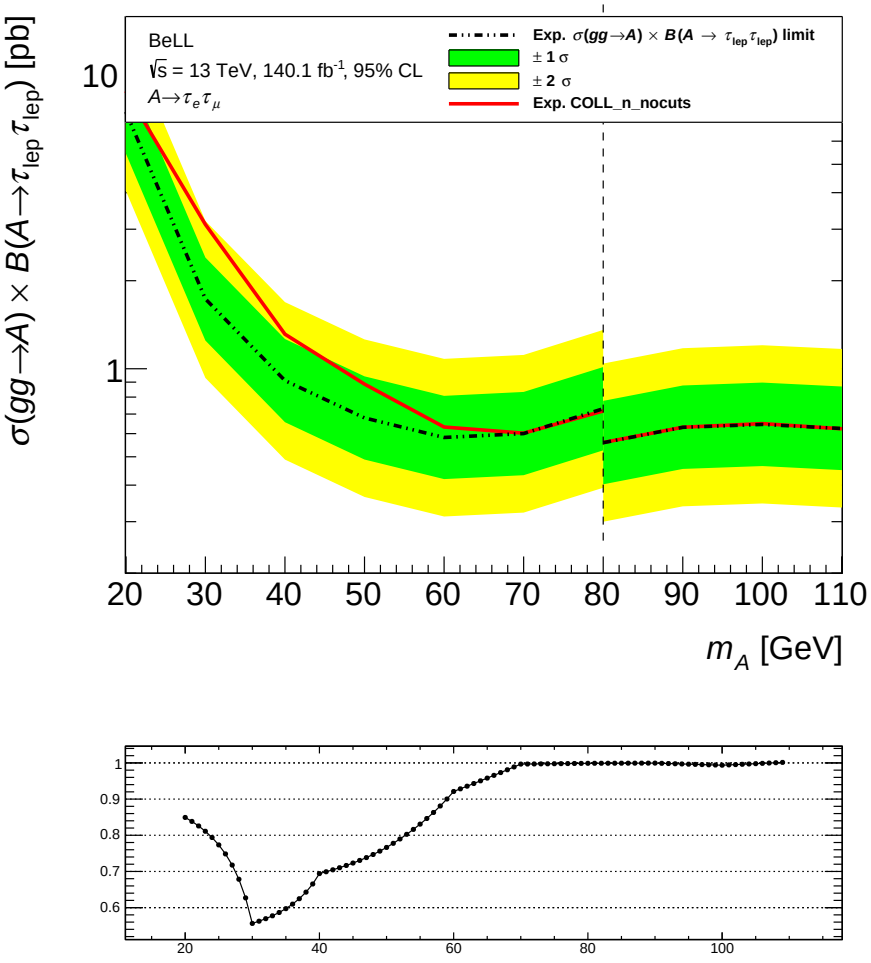

Figure 6.12: Upper limits with and without the $E_{\mathrm{T}}^{\mathrm{miss}} > 60$ GeV cut on the $gg \to A$ production cross-section times the branching ratio for an A boson decay into two τ-leptons, which further decay into a μe, $\mu\mu$ or ee final state for A boson masses from 20 to 80 GeV. The dash-dotted line shows limit with the cut and with its 1σ and 2σ uncertainty bands in green and yellow. The solid red line shows the limit without any additionally implemented cuts (reference). The vertical dashed line indicates the splitting of the SR: only the low-mass hypotheses on the left side are being cut optimized in this work. The ratio plot beneath the limit plot shows the improvement or the deterioration of the limit (dashed line) in comparison to the reference (red line). The y-axis is plotted as: ratio $= \frac{\text{limit}}{\text{reference}}$, with $y = 1$ being the perfect agreement between the limit with the additional cut and the reference. The deviations of 1 indicate whether the limit has improved ($y < 1$) or deteriorated ($y > 1$) in comparison to the reference limit.

Higgs Transverse Momentum Cut

In Figure 6.13a the $p_{\mathrm{T}}^{\mathrm{higgs}}$ variable is shown. This variable is cut with $p_{\mathrm{T}}^{\mathrm{higgs}} > 100$ GeV and visualized in Figure 6.13b. The cut leads to an improvement of up to 48% in comparison to the upper limit without any additional cuts, with the highest improvement being at 30 GeV (Figure 6.14). If the cut is set any lower such as $p_{\mathrm{T}}^{\mathrm{higgs}} > 90$ GeV the limit deteriorates slightly up to 5% between 30 GeV and 80 GeV. However, in the lower mass ranges between 20 GeV and 30 GeV an improvement of up to 6% can be seen. Since this is a much smaller mass range the $p_{\mathrm{T}}^{\mathrm{higgs}} > 100$ GeV cut is kept. If the cut is set higher at $p_{\mathrm{T}}^{\mathrm{higgs}} > 110$ GeV the limit deteriorates up to 20%, especially in the lower ranges compared to the $p_{\mathrm{T}}^{\mathrm{higgs}} > 110$ GeV cut. An slight improvement with up to 7% can be seen in the higher mass ranges. The limit plots for the comparison cuts are shown in the Appendix A.6.

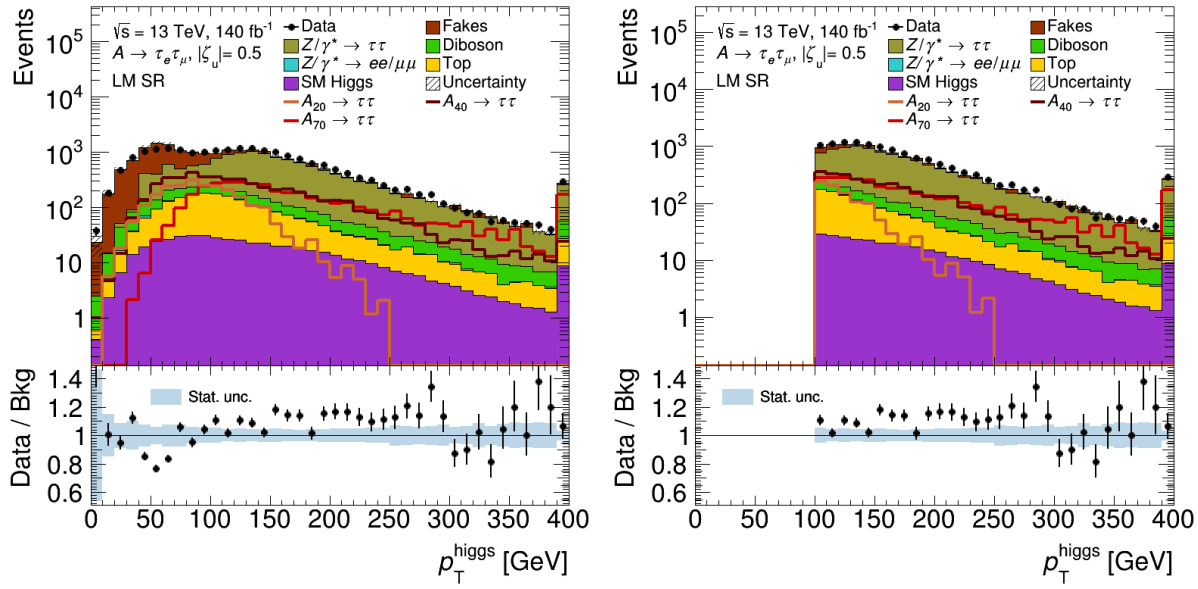

(a) (b)

Figure 6.13: Distribution of the $p_{\mathrm{T}}^{\mathrm{higgs}}$ variable without (6.13a) and with (6.13b) the $p_{\mathrm{T}}^{\mathrm{higgs}} > 100$ cut, shown between 0 GeV and 400 GeV in bins of 10 GeV. The various colors in the stacked histograms show contributions from various background processes and the $A \to \tau\tau$ signal are presented as lines in shades of red for different mass hypotheses. The last bin is used as an overflow bin. The scale used for the number of events in the plots is logarithmic. The blue band in the ratio plot shows the uncertainties from statistical sources.

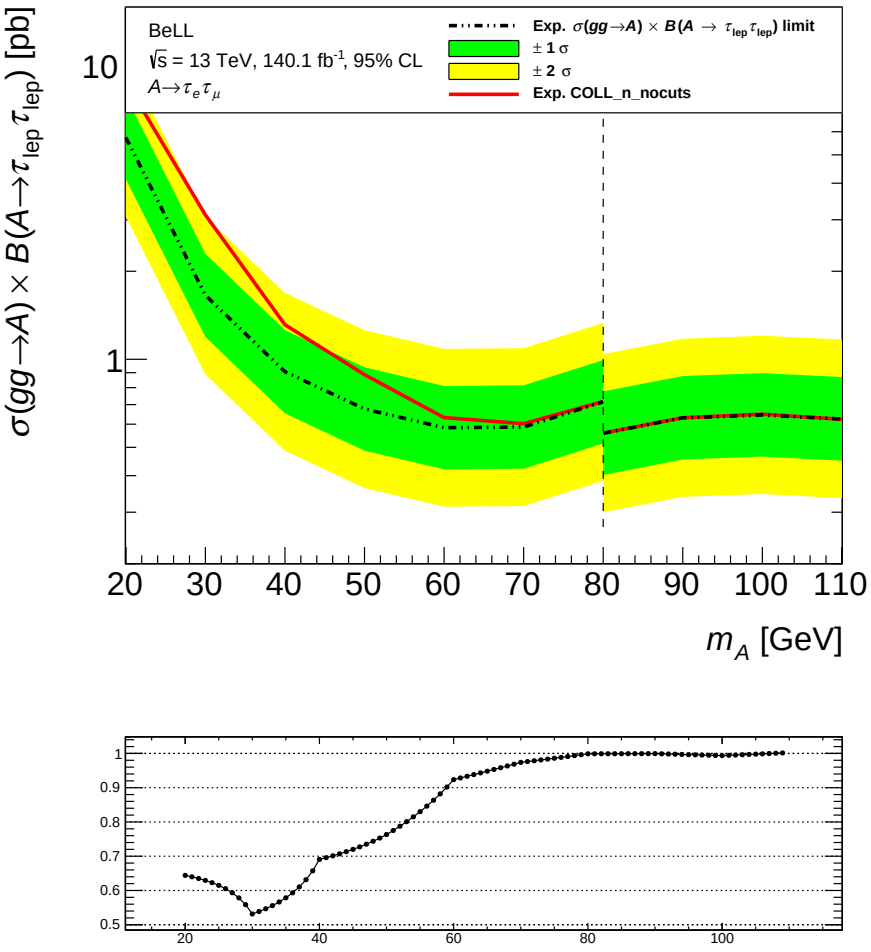

Figure 6.14: Upper limits with and without the $p_{\mathrm{T}}^{\mathrm{higgs}} > 100$ GeV cut on the $gg \to A$ production cross-section times the branching ratio for an A boson decay into two τ-leptons, which further decay into a μe, $\mu\mu$ or ee final state for A boson masses from 20 to 80 GeV. The dash-dotted line shows limit with the cut and with its 1σ and 2σ uncertainty bands in green and yellow. The solid red line shows the limit without any additionally implemented cuts (reference). The vertical dashed line indicates the splitting of the SR: only the low-mass hypotheses on the left side are being cut optimized in this work. The ratio plot beneath the limit plot shows the improvement or the deterioration of the limit (dashed line) in comparison to the reference (red line). The y-axis is plotted as: ratio $= \frac{\text{limit}}{\text{reference}}$, with $y = 1$ being the perfect agreement between the limit with the additional cut and the reference. The deviations of 1 indicate whether the limit has improved ($y < 1$) or deteriorated ($y > 1$) in comparison to the reference limit.

Jet Transverse Momentum Cut

In Figure 6.15a the distribution of the variable $p_{\mathrm{T}}^{\mathrm{jet}}$ is shown. This variable is cut with $p_{\mathrm{T}}^{\mathrm{jet}} > 25$ GeV and visualized in Figure 6.15b. This cut shows an overall optimization of the upper limit in comparison to the upper limit without any additional cuts (Figure 6.16). The improvement is consistent at around 30% in all mass ranges.
If the cut is set higher at $p_{\mathrm{T}}^{\mathrm{jet}} > 40$ GeV a deterioration of up to 9% occurs. Because the cut is already set relatively low, a lower cut is not sensible. The limit plot for the comparison cut is shown in the Appendix A.7.

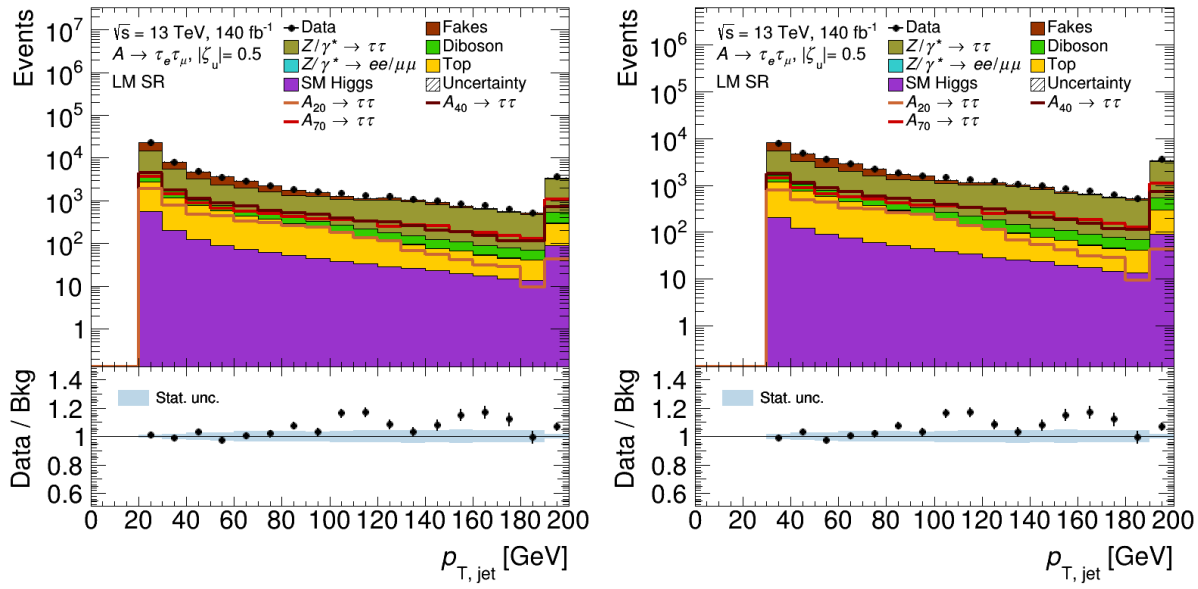

(a) (b)

Figure 6.15: Distribution of the $p_{\mathrm{T}}^{\mathrm{jet}}$ variable without (6.5a) and with (6.5b) the $p_{\mathrm{T}}^{\mathrm{jet}} > 30$ GeV cut, shown between 20 GeV and 200 GeV in bins of 10 GeV. The various colors in the stacked histograms show contributions from various background processes and the $A \to \tau\tau$ signal are presented as lines in shades of red for different mass hypotheses. The last bin is used as an overflow bin. The scale used for the number of events in the plots is logarithmic. The blue band in the ratio plot shows the uncertainties from statistical sources.

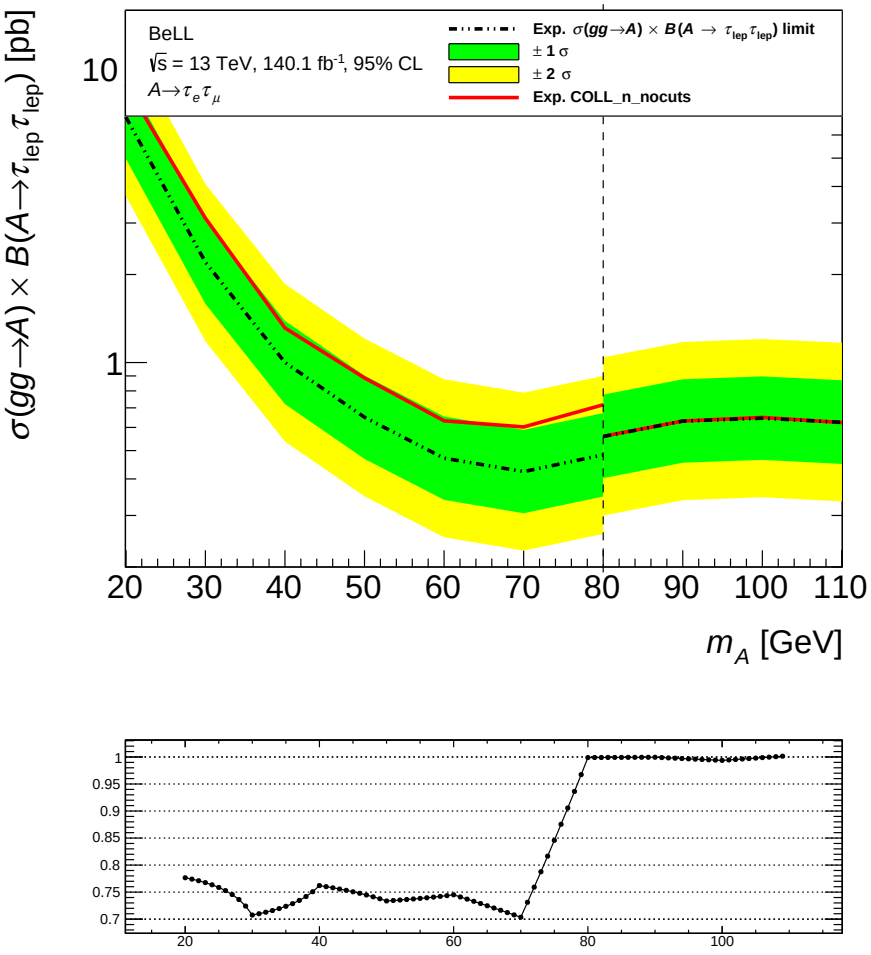

Figure 6.16: Upper limits with and without the $p_{\mathrm{T}}^{\mathrm{jet}} > 30$ GeV cut on the $gg \to A$ production cross-section times the branching ratio for an A boson decay into two τ-leptons, which further decay into a μe, $\mu\mu$ or ee final state for A boson masses from 20 to 80 GeV. The dash-dotted line shows limit with the cut and with its 1σ and 2σ uncertainty bands in green and yellow. The solid red line shows the limit without any additionally implemented cuts (reference). The vertical dashed line indicates the splitting of the SR: only the low-mass hypotheses on the left side are being cut optimized in this work. The ratio plot beneath the limit plot shows the improvement or the deterioration of the limit (dashed line) in comparison to the reference (red line). The y-axis is plotted as: ratio $= \frac{\text{limit}}{\text{reference}}$, with $y = 1$ being the perfect agreement between the limit with the additional cut and the reference. The deviations of 1 indicate whether the limit has improved ($y < 1$) or deteriorated ($y > 1$) in comparison to the reference limit.

$\Delta R_{\text{lep,lep}}$ Cut

The distribution of the $\Delta R_{\text{lep,lep}}$ variable is shown in Figure 6.17a. This variable is cut with $\Delta R_{\text{lep,lep}} < 0.6$ and visualized in Figure 6.17b. This cut ensures an improvement in all mass ranges in comparison to the limit without any additional cuts (Figure 6.18). The greatest optimization can be seen around 30 GeV with 52%. If the cut is set at $\Delta R_{\text{lep,lep}} < 0.4$ the limit deteriorates up to 39% and if the cut is set higher at $\Delta R_{\text{lep,lep}} < 0.8$ the limit deteriorates up to 25%. However a small improvement at around 70 GeV of up to 4% can be seen. The limit plots of the comparison cuts are shown in the Appendix A.8.

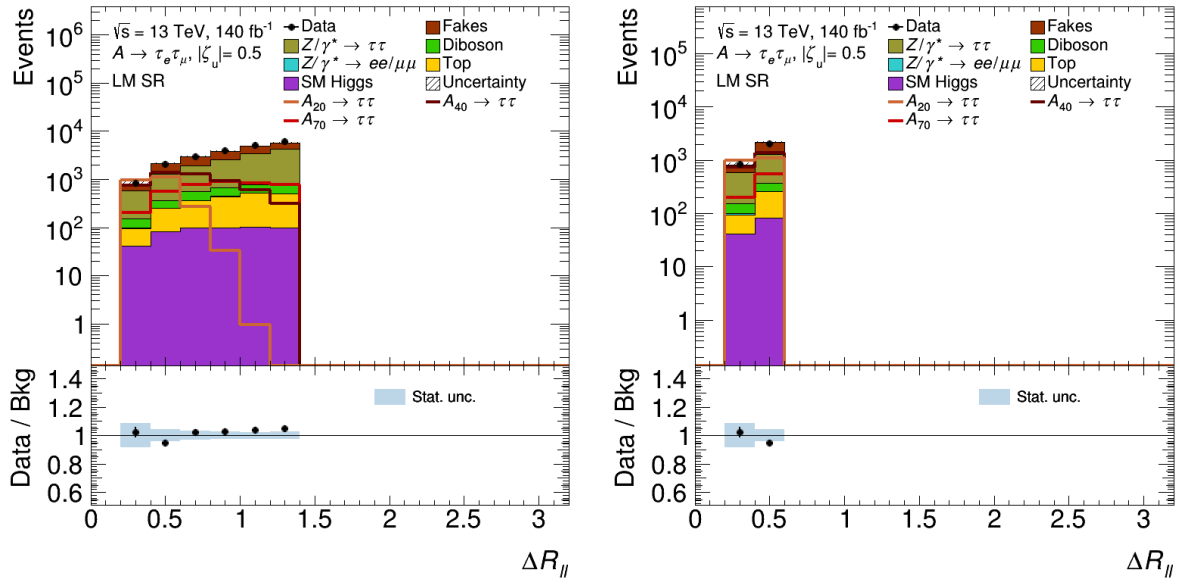

(a) (b)

Figure 6.17: Distribution of the $\Delta R_{\text{lep,lep}}$ variable without (6.17a) and with (6.17b) the $\Delta R_{\text{lep,lep}} < 0.6$ cut, shown between 0.2 and 1.4 in bins of 0.2. This variable has no unit. The various colors in the stacked histograms show contributions from various background processes and the $A \to \tau\tau$ signal are presented as lines in shades of red for different mass hypotheses. The last bin is used as an overflow bin. The scale used for the number of events in the plots is logarithmic. The blue band in the ratio plot shows the uncertainties from statistical sources.

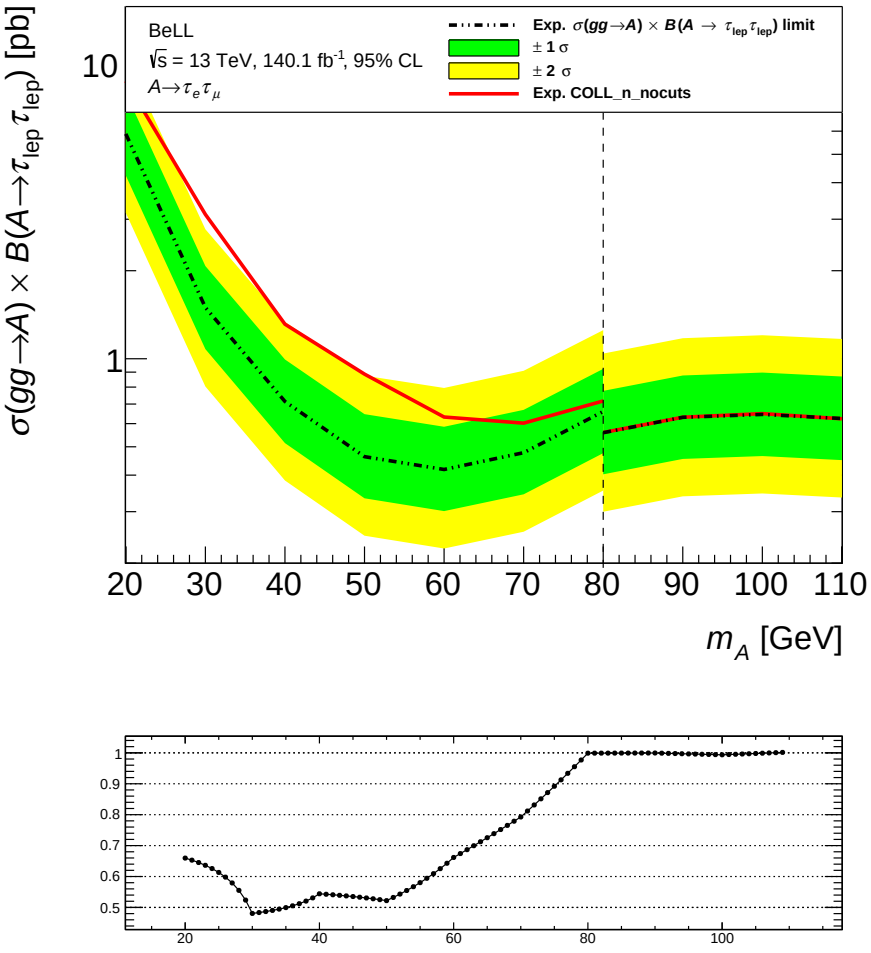

Figure 6.18: Upper limits with and without the $\Delta R_{\text{lep,lep}} < 0.6$ cut on the $gg \to A$ production cross-section times the branching ratio for an A boson decay into two τ-leptons, which further decay into a μe, $\mu\mu$ or ee final state for A boson masses from 20 to 80 GeV. The dash-dotted line shows limit with the cut and with its 1σ and 2σ uncertainty bands in green and yellow. The solid red line shows the limit without any additionally implemented cuts (reference). The vertical dashed line indicates the splitting of the SR: only the low-mass hypotheses on the left side are being cut optimized in this work. The ratio plot beneath the limit plot shows the improvement or the deterioration of the limit (dashed line) in comparison to the reference (red line). The y-axis is plotted as: ratio $= \frac{\text{limit}}{\text{reference}}$, with $y = 1$ being the perfect agreement between the limit with the additional cut and the reference. The deviations of 1 indicate whether the limit has improved ($y < 1$) or deteriorated ($y > 1$) in comparison to the reference limit.

Combined COLL Cuts

In Figure 6.19b, the COLL mass variable $m_{\tau\tau}^{\text{coll}}$ is depicted with all the mentioned cuts, which means that all the background and signal events that do not meet the criteria of $E_{\text{T}}^{\text{miss}} > 60$ GeV, $p_{\text{T}}^{\text{higgs}} > 100$ GeV, $p_{\text{T}}^{\text{jet}} > 40$ GeV and $\Delta R_{\text{lep,lep}} < 0.6$ are cut. An improvement of the background-to-signal ratio can be seen in comparison to Figure 6.19a, which shows the variable $m_{\tau\tau}^{\text{coll}}$ without any additional cuts. The limit and ratio plot for all the mentioned cuts combined, are depicted in Figure 6.20. In total, a large improvement can be seen in comparison to the limit without any additional cuts. However, the largest optimization of the upper limit with around 68% can be found at 30 GeV and 50 GeV. The improvements are relatively constant in all the mass ranges and vary slightly between 50% at 70 GeV and 45% at 20 GeV.

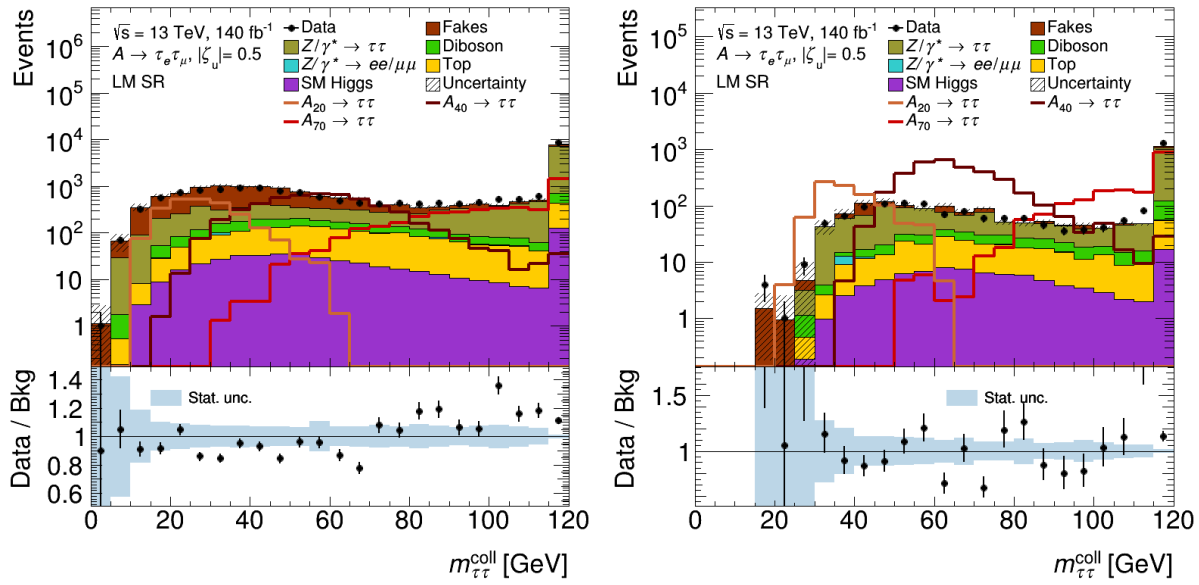

(a) (b)

Figure 6.19: Distribution of the $m_{\tau\tau}^{\text{coll}}$ variable without (a) and with (b) the combined cuts ($E_{\text{T}}^{\text{miss}} > 60$ GeV, $p_{\text{T}}^{\text{higgs}} > 100$ GeV, $p_{\text{T}}^{\text{jet}} > 40$ GeV and $\Delta R_{\text{lep,lep}} < 0.6$), shown between 0 GeV and 120 GeV in bins of 5 GeV. The various colors in the stacked histograms show contributions from various background processes and the $A \to \tau\tau$ signal are presented as lines in shades of red for different mass hypotheses. The scale used for the number of events in the plots is logarithmic.The blue band in the ratio plot shows the uncertainties from statistical sources.

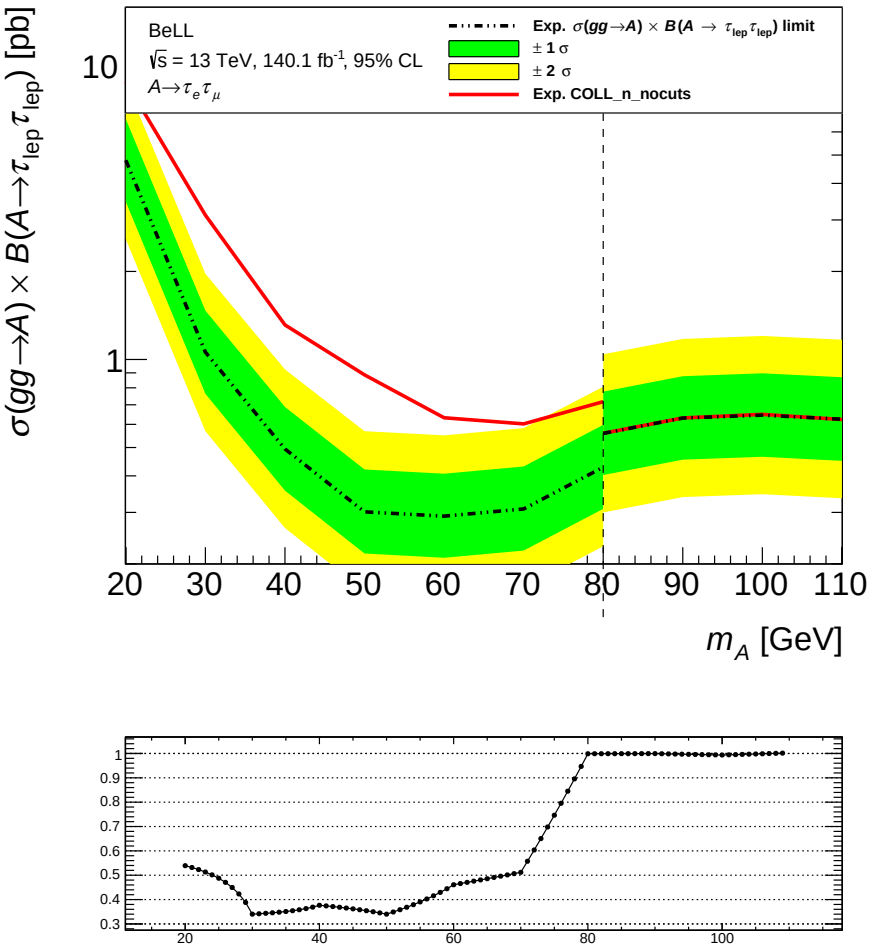

Figure 6.20: Upper limits with and without the combined cuts ($E_{\mathrm{T}}^{\mathrm{miss}} > 50$ GeV, $p_{\mathrm{T}}^{\mathrm{higgs}} > 110$ GeV, $p_{\mathrm{T}}^{\mathrm{jet}} > 30$ GeV and $\Delta R_{\mathrm{lep,lep}} < 0.6$) on the $gg \to A$ production cross-section times the branching ratio for an A boson decay into two τ-leptons, which further decay into a μe, $\mu\mu$ or ee final state for A boson masses from 20 to 80 GeV. The dash-dotted line shows limit with the cuts and with its 1σ and 2σ uncertainty bands in green and yellow. The solid red line shows the limit without any additionally implemented cuts (reference). The vertical dashed line indicates the splitting of the SR: only the low-mass hypotheses on the left side are being cut optimized in this work. The ratio plot beneath the limit plot shows the improvement or the deterioration of the limit (dashed line) in comparison to the reference (red line). The y-axis is plotted as: ratio $= \frac{\text{limit}}{\text{reference}}$, with $y = 1$ being the perfect agreement between the limit with the additional cuts and the reference. The deviations of 1 indicate whether the limit has improved ($y < 1$) or deteriorated ($y > 1$) in comparison to the reference limit.

6.3 Comparison between the MMC upper limit and the COLL upper limit

In Figure 6.21 the upper limits for the MMC and COLL mass are depicted. The COLL mass is shown as the reference to compare the two limits with each other. In the mass ranges between 20 GeV and 50 GeV the MMC mass has a limit that is up to 20% better than the limit of the COLL mass. On the other hand, the COLL mass has a up to 12% better limit in the higher mass ranges between 50 GeV and 80 GeV. One reason why the COLL mass performs better in the higher mass ranges is, that this method tends to overestimate the mass of the $\tau\tau$-pairs and therefore over estimates the mass of the A boson. However, the main reason why the COLL mass performs better in the higher mass ranges is that the COLL mass approximation reconstructs the Z peak less well, because Z events are rarely collinear. This causes the peak of the Z boson being narrower for the MMC mass approximation, than for the COLL mass approximation. The MMC mass has therefore a better limit far away from the peak. On the other hand, closer to the Z peak the limit deteriorates in comparison to the COLL mass. Over all the MMC cuts produce a slightly better limit, because the MMC technique delivers an improved reconstruction of the invariant mass compared to the COLL mass, as explained in chapter 4.5 "Invariant Mass Reconstruction Methods". However both limits show a similar improvement.
The optimized cuts for the MMC mass and COLL mass are almost identical and only the $p_{\mathrm{T}}^{\mathrm{higgs}}$ differs slightly ($\Delta p_{\mathrm{T}}^{\mathrm{higgs}} = 10$ GeV) because of the different reconstruction methods. The different cuts can be seen in Table 6.1.

	MMC cuts	COLL cuts
$E_{\mathrm{T}}^{\mathrm{miss}}$	> 50 GeV	
$p_{\mathrm{T}}^{\mathrm{higgs}}$	> 110 GeV	> 100 GeV
$p_{\mathrm{T}}^{\mathrm{jet}}$	> 30 GeV	
$\Delta R_{\mathrm{lep,lep}}$	< 0.6	

Table 6.1: Overview of the selection criteria for the MMC and the COLL mass.

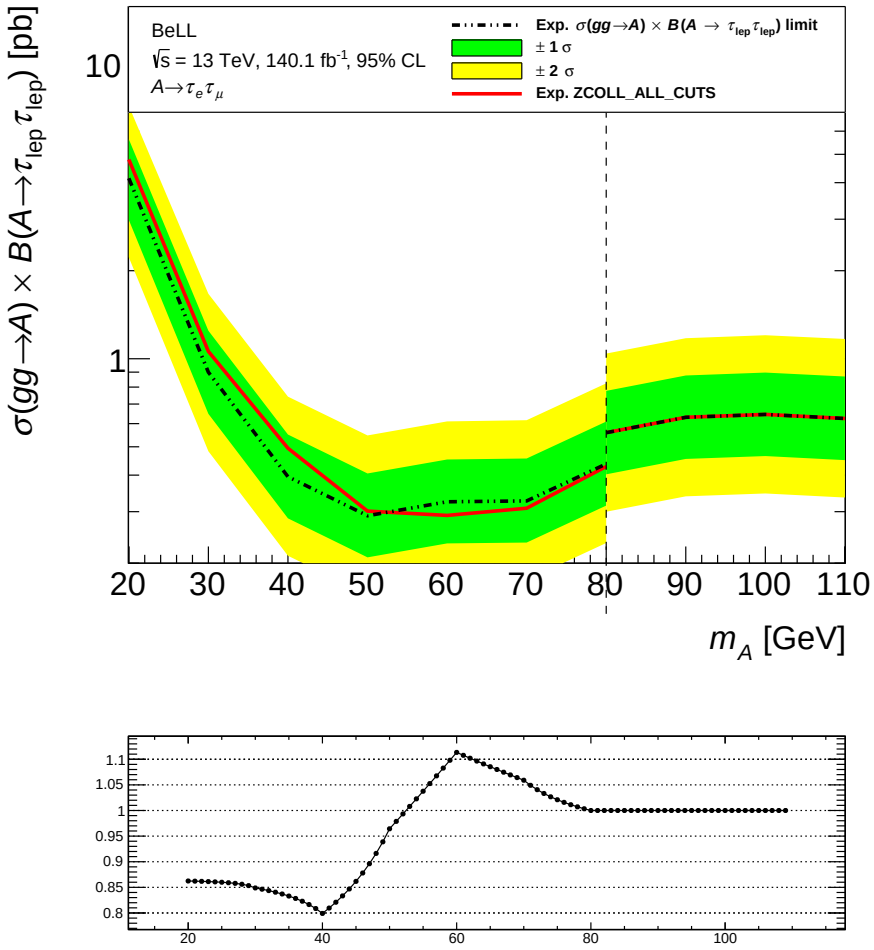

Figure 6.21: Upper limits of the MMC mass (dotted line) and the COLL mass (red solid line) with cuts ($E_{\mathrm{T}}^{\mathrm{miss}} > 50$ GeV, $p_{\mathrm{T}}^{\mathrm{higgs}} > 110/100$ GeV, $p_{\mathrm{T}}^{\mathrm{jet}} > 30$ GeV and $\Delta R_{\mathrm{lep,lep}} < 0.6$) on the $gg \to A$ production cross-section times the branching ratio for an A boson decay into two τ-leptons, which further decay into a μe, $\mu\mu$ or ee final state for A boson masses from 20 to 80 GeV. The dash-dotted line shows limit with its 1σ and 2σ uncertainty bands in green and yellow. The vertical dashed line indicates the splitting of the SR: only the low-mass hypotheses on the left side are being cut optimized in this work. The ratio plot beneath the limit plot shows the improvement or the deterioration of the limit (dashed line) in comparison to the reference (red line). The y-axis is plotted as: ratio $= \frac{\text{limit}}{\text{reference}}$, with $y = 1$ being the perfect agreement between the MMC limit and the COLL limit. The deviations of 1 indicate whether the limit has improved ($y < 1$) or deteriorated ($y > 1$) in comparison to the reference limit.

7 Summary

In this thesis the basic principles of a search for a low-mass CP-odd A boson as well as the motivation behind the search have been presented. Especially the decay channel $A \to \tau\tau$ was looked at. The chosen decay channel, for this analysis, was the leptonic decay of the two τ-leptons into an electron and muon. Corresponding to this decay channel, different background processes with the same final state have been presented. Different event selection criteria have been tested and then used to optimize the upper limit for the $\sigma(gg \to A) \times B(A \to \tau_{\text{lep}}\tau_{\text{lep}})$. This has been done for two mass reconstruction methods: the collinear mass approximation (COLL) and the missing mass calculator (MMC). The cuts that improve the significance of the A boson signal the most, while using the MMC, are $E_{\text{T}}^{\text{miss}} > 60$ GeV, $p_{\text{T}}^{\text{higgs}} > 110$ GeV, $p_{\text{T}}^{\text{jet}} > 30$ GeV and $\Delta R_{\text{lep,lep}} < 0.6$. In comparison to the upper limit without any additional cuts a large improvement can be seen. However the improvement varies depending on the mass range between 30% and 70%. The cuts which strengthen the A boson signal, while using the COLL mass reconstruction method are almost identical to the MMC cuts, but they produce a different upper limit. The cuts for the COLL mass are: $E_{\text{T}}^{\text{miss}} > 60$ GeV, $p_{\text{T}}^{\text{higgs}} > 100$ GeV, $p_{\text{T}}^{\text{jet}} > 30$ GeV and $\Delta R_{\text{lep,lep}} < 0.6$. The improvement is more constant and only varies between 45% and 68%.

The comparison of the upper limits of the two mass reconstruction methods shows that the MMC mass performs better in the lower mass ranges, while the COLL mass performs better in the higher mass ranges. However overall the MMC mass provides a slightly better upper limit.

To further improve the overall upper limit, a combination of the MMC and COLL upper limit could be a solution.

References

[1] G. Aad et al. "The ATLAS Experiment at the CERN Large Hadron Collider". In: *Journal of Instrumentation* 3.08 (2008), S08003. DOI: 10.1088/1748-0221/3/08/S08003.

[2] D. P. Aguillard and et al. (Muon g 2 Collaboration). "Measurement of the Positive Muon Anomalous Magnetic Moment to 0.20 ppm". In: *Physical Review Letters* 131 (2023), p. 161802.

[3] R. Alkofer and J. Greensite. "Quark Confinement: The Hard Problem of Hadron Physics". In: *Journal of Physics G: Nuclear and Particle Physics* 34.7 (2007), S2. DOI: 10.1088/0954-3899/34/7/S02.

[4] Chittaranjan Andrade. "The P Value and Statistical Significance: Misunderstandings, Explanations, Challenges, and Alternatives". In: *Indian Journal of Psychological Medicine* 41.3 (2019), pp. 210–215. DOI: 10.4103/IJPSYM.IJPSYM_193_19. URL: https://doi.org/10.4103/IJPSYM.IJPSYM_193_19.

[5] T. Aoyama and et al. "The anomalous magnetic moment of the muon in the Standard Model". In: *Physics Reports* 887 (2020), p. 1.

[6] ATLAS Collaboration. *Statistical Significance - ATLAS Cheat Sheet*. Accessed: 2024-10-29. 2023. URL: https://cds.cern.ch/record/2875522/files/Statistical%20Significance%20-%20ATLAS%20Cheat%20Sheet.pdf.

[7] ATLAS Collaboration. *Vertex Reconstruction Performance of the ATLAS Detector at s = 13 TeV*. ATL-PHYS-PUB 2015-026. CERN, 2015. URL: https://cds.cern.ch/record/2037717.

[8] G. W. Bennett and et al. "Final report of the E821 muon anomalous magnetic moment measurement at BNL". In: *Physical Review D* 73 (2006). Muon g 2 Collaboration, p. 072003.

[9] CERN. *ATLAS and CMS experiments submit Higgs search papers*. Accessed: 2024-10-29. Feb. 2012. URL: https://home.cern/news/press-release/cern/atlas-and-cms-experiments-submit-higgs-search-papers.

[10] CERN. *Facts and Figures about the LHC*. Accessed: 2024-10-07. URL: https://home.cern/resources/faqs/facts-and-figures-about-lhc.

[11] CERN Courier. "Lattice calculations start to clarify muon g-2". In: *CERN Courier* (2023). Accessed: 2023-10-29. URL: https://cerncourier.com/a/lattice-calculations-start-to-clarify-muon-g-2/.

[12] ATLAS Collaboration. *ATLAS detector and physics performance: Technical Design Report, 1*. Technical design report. ATLAS. Geneva: CERN, 1999. URL: https://cds.cern.ch/record/391176.

[13] ATLAS Collaboration. "Observation of a new particle in the search for the Standard Model Higgs boson with the ATLAS detector at the LHC". In: *Physics Letters B* 716 (2012), pp. 1–29. DOI: 10.1016/j.physletb.2012.08.020. arXiv: 1207.7214.

[14] ATLAS Collaboration. *Search for a light CP-odd Higgs boson decaying into a pair of τ-leptons in proton-proton collisions at $\sqrt{s} = 13$ TeV with the ATLAS detector*. Sept. 2024. eprint: 2409.20381.

[15] ATLAS Collaboration. "The ATLAS experiment at the CERN Large Hadron Collider: a description of the detector configuration for Run 3". In: *Journal of Instrumentation* 19.05 (May 2024). DOI: 10.1088/1748-0221/19/05/P05063. URL: https://dx.doi.org/10.1088/1748-0221/19/05/P05063.

[16] CERN Collaboration. *Standard Model of Elementary Particles - Visualization*. Accessed: 2024-11-23. 2015. URL: https://cds.cern.ch/record/2012465/plots.

[17] Wikipedia Contributors. *Standard Model of Elementary Particles*. Accessed: 2024-11-23. 2024. URL: https://en.wikipedia.org/wiki/File:Standard_Model_of_Elementary_Particles.svg.

[18] E. Corbelli and P. Salucci. "The extended rotation curve and the dark matter halo of M33". In: *Monthly Notices of the Royal Astronomical Society* 311 (2000), p. 441.

[19] G. Cowan et al. "Asymptotic formulae for likelihood-based tests of new physics". In: *The European Physical Journal C* 71.2 (2011), p. 1554. DOI: 10.1140/epjc/s10052-011-1554-0.

[20] Glen Cowan. *Some Statistical Tools for Particle Physics*. Particle Physics Colloquium, MPI für Physik u. Astrophysik, Munich. Available at https://www.pp.rhul.ac.uk/~cowan/stat/cowan_munich16.pdf. Physics Department, Royal Holloway, University of London, May 2016.

[21] S. Davidson and H. E. Haber. "Basis-independent methods for the two-Higgs-doublet model". In: *Physical Review D* 72 (2005). DOI: 10.1103/PhysRevD.72.035004.

[22] J.E. Dodd and B. Gripaios. *The Ideas of Particle Physics*. Cambridge University Press, 2020. ISBN: 9781108727402.

[23] A. Elagin et al. "A new mass reconstruction technique for resonances decaying to". In: *Nuclear Instruments and Methods in Physics Research Section A: Accelerators, Spectrometers, Detectors and Associated Equipment* 654.1 (Oct. 2011), pp. 481–489. ISSN: 0168-9002. DOI: 10.1016/j.nima.2011.07.009. URL: http://dx.doi.org/10.1016/j.nima.2011.07.009.

[24] M. B. Gavela et al. "Standard Model CP-violation and baryon asymmetry". In: *Modern Physics Letters A* 09 (1994), p. 795.

[25] Julia Gonski. *What happens when energy goes missing?* Accessed: 2024-12-08. Nov. 2023. URL: https://atlas.cern/updates/blog/what-happens-when-energy-goes-missing.

[26] E. Gross. “Practical Statistics for High Energy Physics”. In: *CERN Yellow Reports: Proceedings of the 2017 European School of High-Energy Physics*. Vol. 3. CERN, 2018, pp. 197–228. DOI: 10.23730/CYRSP-2018-003.197.

[27] Hannah Jacobi. “Improvements of the Search for a Light CP-Odd Higgs Boson Decaying to a Pair of Tau Leptons Using Artificial Neural Networks”. Master’s Thesis. Dresden, Germany: Technische Universität Dresden, 2023.

[28] Tom Kreße. “Search for a light CP-odd Higgs boson decaying into a pair of τ-leptons with the ATLAS detector”. Master’s thesis. Dresden, Germany: Technische Universität Dresden, 2024.

[29] Tom W. B. Kribbel. “The Standard Model of Particle Physics”. In: *European Review* 23.1 (2015). DOI: 10.1017/S1062798714000520.

[30] A. D. Martin et al. “Uncertainties on global PDF analyses and implications for predicted hadronic cross sections”. In: *Eur. Phys. J. C* 64 (2009), p. 653. DOI: 10.1140/epjc/s10052-009-1164-2. arXiv: 0905.3531 [hep-ph].

[31] Paul Moder. “Search for a light CP-odd Higgs boson decaying into a pair”. Master’s thesis. Dresden, Germany: Technische Universität Dresden, May 2024.

[32] Claudio Pfammatter. *Monte Carlo Methoden: Numerische Verfahren zum Lösen praxisorientierter Probleme*. Maturaarbeit, Kollegium Spiritus Sanctus Brig. Dec. 2019.

[33] Gavin P. Salam. “Towards jetography”. In: *The European Physical Journal C* 67.3 (June 1, 2010), pp. 637–686. DOI: 10.1140/epjc/s10052-010-1314-6. URL: https://doi.org/10.1140/epjc/s10052-010-1314-6.

[34] Frank Wilczek. “Nobel Lecture: Asymptotic freedom: From paradox to paradigm”. In: *Reviews of Modern Physics* 77.3 (Sept. 2005), pp. 857–870. ISSN: 1539-0756. DOI: 10.1103/revmodphys.77.857. URL: http://dx.doi.org/10.1103/RevModPhys.77.857.

A Appendix

A.1 $E_{\mathrm{T}}^{\mathrm{miss}}$ MMC Limit Plots

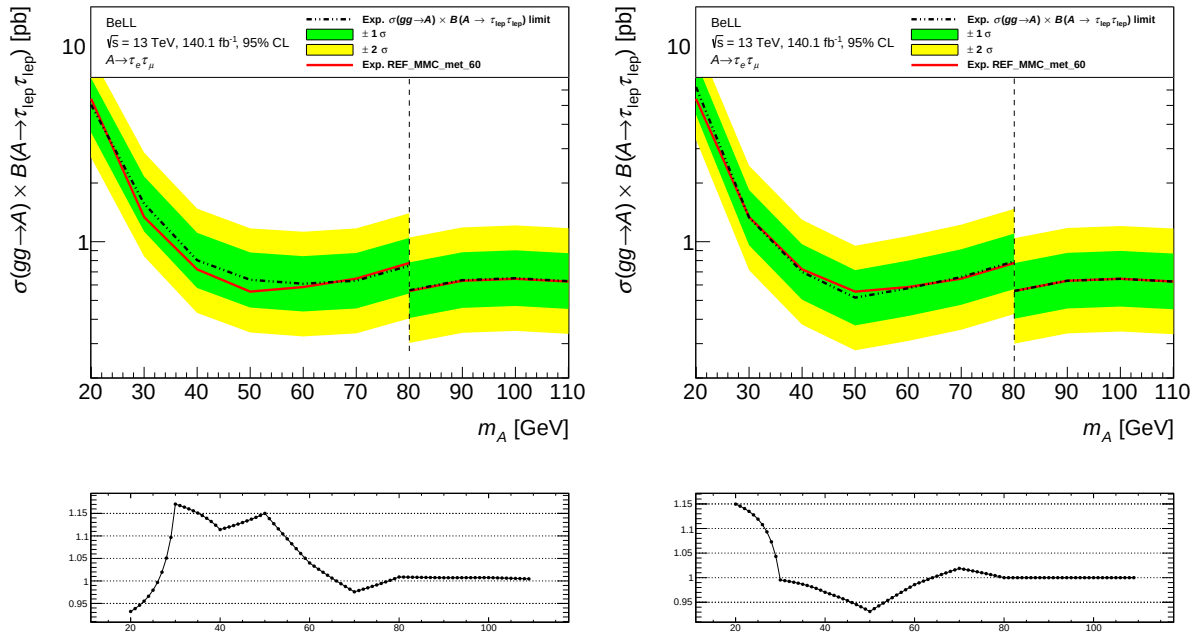

(a) (b)

Figure A.1: Upper limits of the $E_{\mathrm{T}}^{\mathrm{miss}} > 50$ GeV cut (A.1a) and the $E_{\mathrm{T}}^{\mathrm{miss}} > 70$ GeV cut (A.1b) on the $gg \to A$ production cross-section times the branching ratio for an A boson decay into two τ-leptons, which further decay into a μe, $\mu\mu$ or ee final state for A boson masses from 20 to 80 GeV. The dash-dotted line shows limit with the cuts and with its 1σ and 2σ uncertainty bands in green and yellow. The solid red line shows the limit of the chosen $E_{\mathrm{T}}^{\mathrm{miss}} > 60$ GeV cut (reference). The vertical dashed line indicates the splitting of the SR: only the low-mass hypotheses on the left side are being cut optimized in this work. The ratio plot beneath the limit plot shows the improvement or the deterioration of the limit (dashed line) in comparison to the reference (red line). The y-axis is plotted as: ratio $= \frac{\text{limit}}{\text{reference}}$, with $y = 1$ being the perfect agreement between the limit with the additional cut and the reference. The deviations of 1 indicate whether the limit has improved ($y < 1$) or deteriorated ($y > 1$) in comparison to the reference limit.

A.2 $p_{\mathrm{T}}^{\mathrm{higgs}}$ MMC Limit Plot

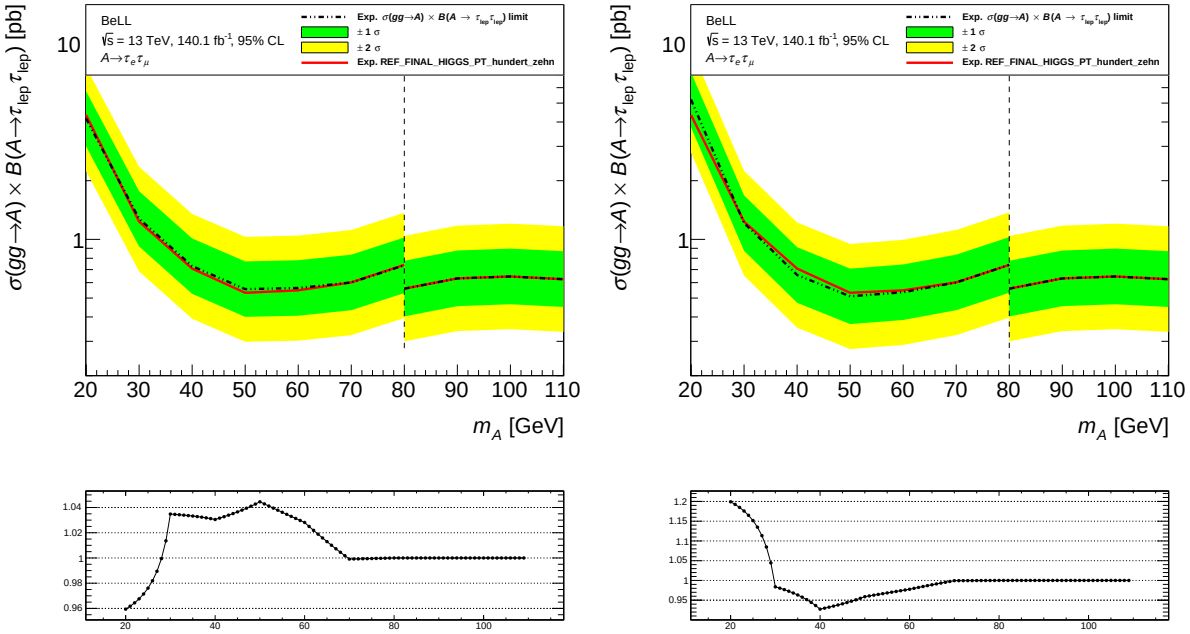

(a) (b)

Figure A.2: Upper limits of the $p_{\mathrm{T}}^{\mathrm{higgs}} > 100$ GeV cut (A.2a) and the $p_{\mathrm{T}}^{\mathrm{higgs}} > 120$ GeV cut (A.2b) on the $gg \to A$ production cross-section times the branching ratio for an A boson decay into two τ-leptons, which further decay into a μe, $\mu\mu$ or ee final state for A boson masses from 20 to 80 GeV. The dash-dotted line shows limit with the cuts and with its 1σ and 2σ uncertainty bands in green and yellow. The solid red line shows the limit of the chosen $p_{\mathrm{T}}^{\mathrm{higgs}} > 110$ GeV cut (reference). The vertical dashed line indicates the splitting of the SR: only the low-mass hypotheses on the left side are being cut optimized in this work. The ratio plot beneath the limit plot shows the improvement or the deterioration of the limit (dashed line) in comparison to the reference (red line). The y-axis is plotted as: ratio $= \frac{\text{limit}}{\text{reference}}$, with $y = 1$ being the perfect agreement between the limit with the additional cut and the reference. The deviations of 1 indicate whether the limit has improved ($y < 1$) or deteriorated ($y > 1$) in comparison to the reference limit.

A.3 $p_{\mathrm{T}}^{\mathrm{jet}}$ MMC Limit Plot

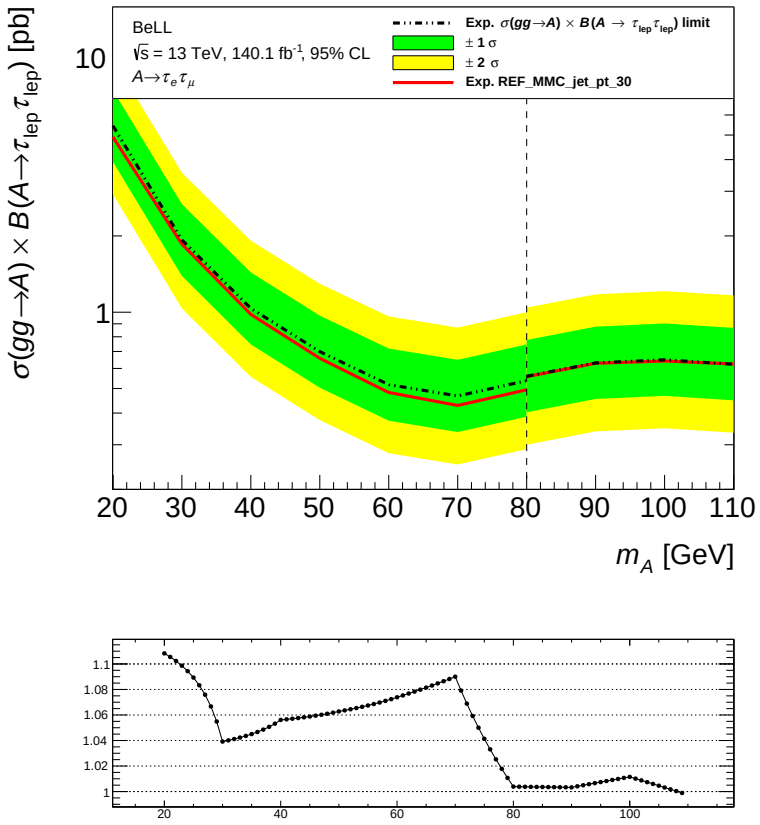

Figure A.3: Upper limits of the $p_t^{\mathrm{jet}} > 40$ GeV on the $gg \to A$ production cross-section times the branching ratio for an A boson decay into two τ-leptons, which further decay into a μe, $\mu\mu$ or ee final state for A boson masses from 20 to 80 GeV. The dash-dotted line shows limit with the cuts and with its 1σ and 2σ uncertainty bands in green and yellow. The solid red line shows the limit with $p_t^{\mathrm{jet}} > 30$ GeV (reference). The vertical dashed line indicates the splitting of the SR: only the low-mass hypotheses on the left side are being cut optimized in this work. The ratio plot beneath the limit plot shows the improvement or the deterioration of the limit (dashed line) in comparison to the reference (red line). The y-axis is plotted as: ratio $= \frac{\text{limit}}{\text{reference}}$, with $y = 1$ being the perfect agreement between the limit with the additional cut and the reference. The deviations of 1 indicate whether the limit has improved ($y < 1$) or deteriorated ($y > 1$) in comparison to the reference limit.

A.4 $\Delta R_{\text{lep,lep}}$ MMC Limit Plots

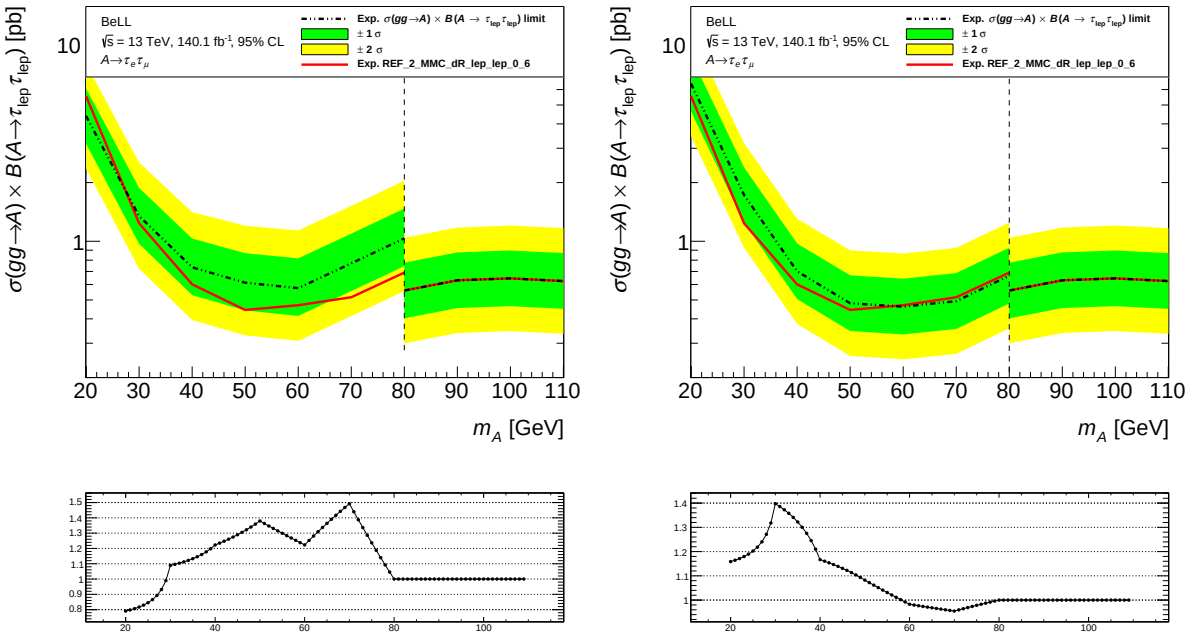

(a) (b)

Figure A.4: Upper limits of the $\Delta R_{\text{lep,lep}} < 0.4$ cut (A.4a) and the $\Delta R_{\text{lep,lep}} < 0.8$ cut (A.4b) on the $gg \to A$ production cross-section times the branching ratio for an A boson decay into two τ-leptons, which further decay into a μe, $\mu\mu$ or ee final state for A boson masses from 20 to 80 GeV. The dash-dotted line shows limit with the cuts and with its 1σ and 2σ uncertainty bands in green and yellow. The solid red line shows the limit of the chosen $\Delta R_{\text{lep,lep}} < 0.6$ cut (reference). The vertical dashed line indicates the splitting of the SR: only the low-mass hypotheses on the left side are being cut optimized in this work. The ratio plot beneath the limit plot shows the improvement or the deterioration of the limit (dashed line) in comparison to the reference (red line). The y-axis is plotted as: ratio $= \frac{\text{limit}}{\text{reference}}$, with $y = 1$ being the perfect agreement between the limit with the additional cut and the reference. The deviations of 1 indicate whether the limit has improved ($y < 1$) or deteriorated ($y > 1$) in comparison to the reference limit.

A.5 $E_{\mathrm{T}}^{\mathrm{miss}}$ COLL Limit Plots

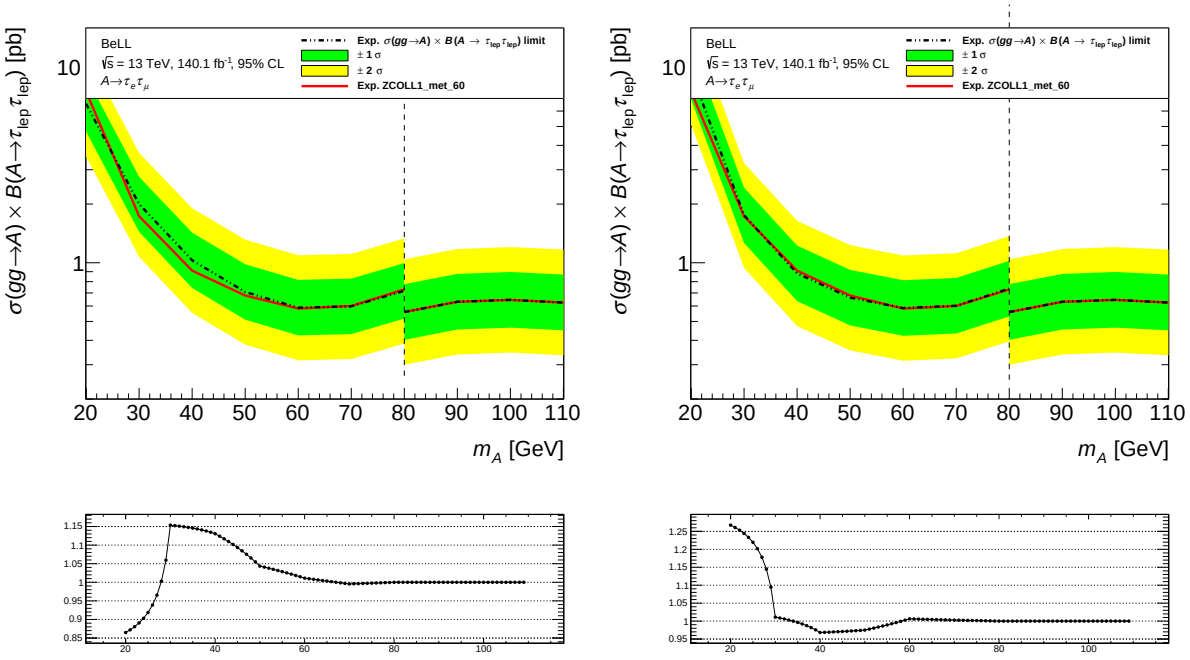

(a) (b)

Figure A.5: Upper limits of the $E_{\mathrm{T}}^{\mathrm{miss}} > 50$ GeV cut (A.5a) and the $E_{\mathrm{T}}^{\mathrm{miss}} > 70$ GeV cut (A.5b) on the $gg \to A$ production cross-section times the branching ratio for an A boson decay into two τ-leptons, which further decay into a μe, $\mu\mu$ or ee final state for A boson masses from 20 to 80 GeV. The dash-dotted line shows limit with the cuts and with its 1σ and 2σ uncertainty bands in green and yellow. The solid red line shows the limit of the chosen $E_{\mathrm{T}}^{\mathrm{miss}} > 60$ GeV cut (reference). The vertical dashed line indicates the splitting of the SR: only the low-mass hypotheses on the left side are being cut optimized in this work. The ratio plot beneath the limit plot shows the improvement or the deterioration of the limit (dashed line) in comparison to the reference (red line). The y-axis is plotted as: ratio $= \frac{\text{limit}}{\text{reference}}$, with $y = 1$ being the perfect agreement between the limit with the additional cut and the reference. The deviations of 1 indicate whether the limit has improved ($y < 1$) or deteriorated ($y > 1$) in comparison to the reference limit.

A.6 $p_{\mathrm{T}}^{\mathrm{higgs}}$ COLL Limit Plot

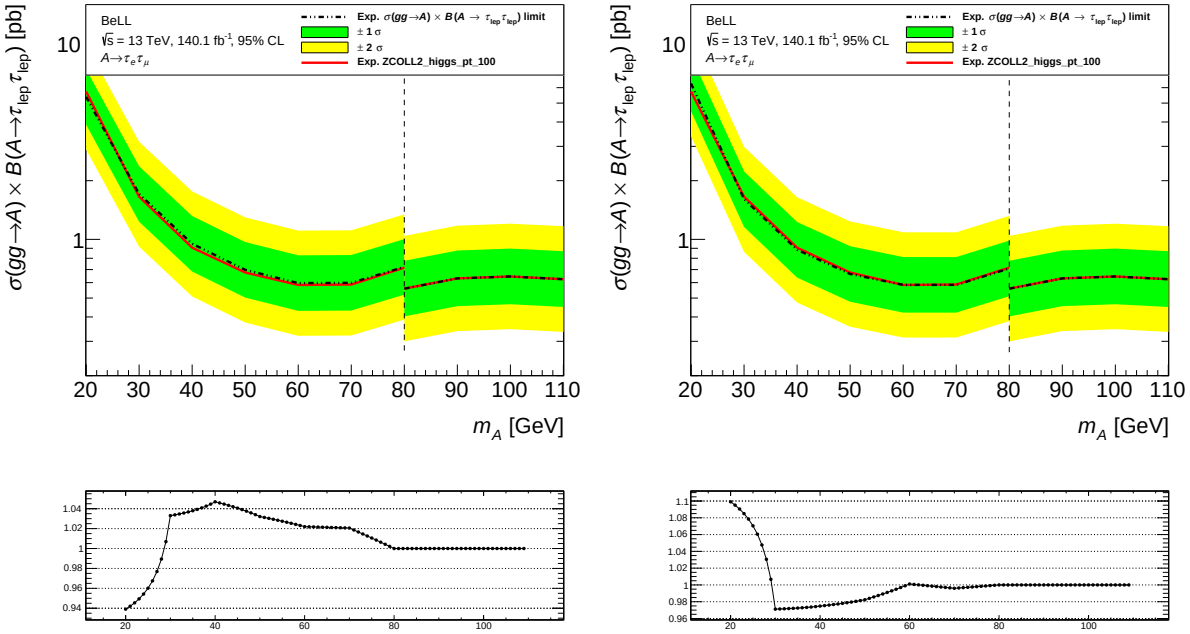

(a) (b)

Figure A.6: Upper limits of the $p_{\mathrm{T}}^{\mathrm{higgs}} > 90$ GeV cut (A.6a) and the $p_{\mathrm{T}}^{\mathrm{higgs}} > 110$ GeV cut (A.6b) on the $gg \to A$ production cross-section times the branching ratio for an A boson decay into two τ-leptons, which further decay into a μe, $\mu\mu$ or ee final state for A boson masses from 20 to 80 GeV. The dash-dotted line shows limit with the cuts and with its 1σ and 2σ uncertainty bands in green and yellow. The solid red line shows the limit of the chosen $p_{\mathrm{T}}^{\mathrm{higgs}} > 100$ GeV cut (reference). The vertical dashed line indicates the splitting of the SR: only the low-mass hypotheses on the left side are being cut optimized in this work. The ratio plot beneath the limit plot shows the improvement or the deterioration of the limit (dashed line) in comparison to the reference (red line). The y-axis is plotted as: ratio $= \frac{\text{limit}}{\text{reference}}$, with $y = 1$ being the perfect agreement between the limit with the additional cut and the reference. The deviations of 1 indicate whether the limit has improved ($y < 1$) or deteriorated ($y > 1$) in comparison to the reference limit.

A.7 $p_{\mathrm{T}}^{\mathrm{jet}}$ COLL Limit Plot

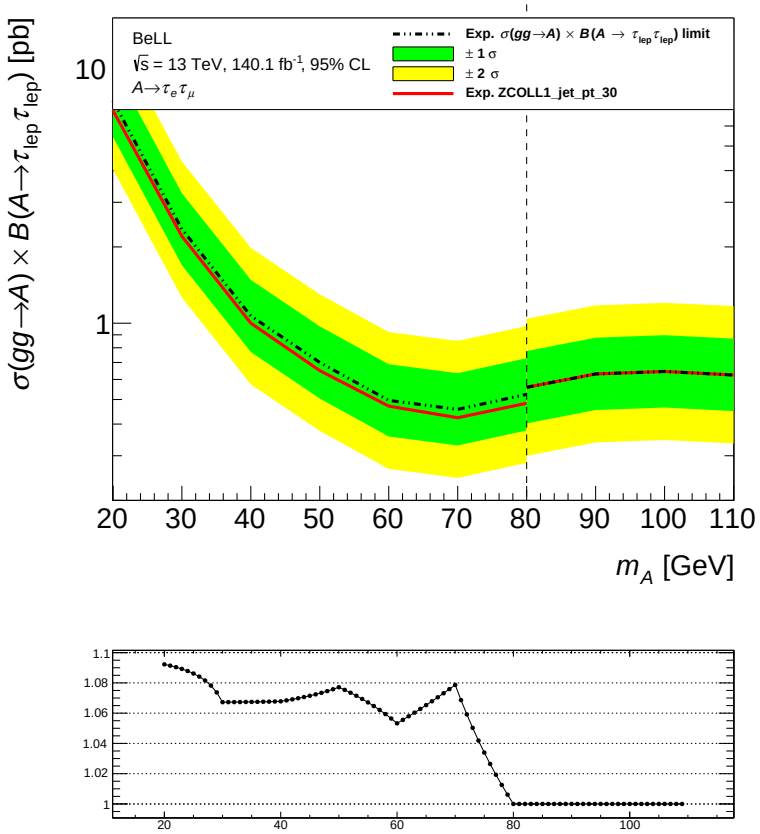

Figure A.7: Upper limits of the $p_t^{\mathrm{jet}} > 40$ GeV on the $gg \to A$ production cross-section times the branching ratio for an A boson decay into two τ-leptons, which further decay into a μe, $\mu\mu$ or ee final state for A boson masses from 20 to 80 GeV. The dash-dotted line shows limit with the cuts and with its 1σ and 2σ uncertainty bands in green and yellow. The solid red line shows the limit with $p_t^{\mathrm{jet}} > 30$ GeV (reference). The vertical dashed line indicates the splitting of the SR: only the low-mass hypotheses on the left side are being cut optimized in this work. The ratio plot beneath the limit plot shows the improvement or the deterioration of the limit (dashed line) in comparison to the reference (red line). The y-axis is plotted as: ratio $= \frac{\text{limit}}{\text{reference}}$, with $y = 1$ being the perfect agreement between the limit with the additional cut and the reference. The deviations of 1 indicate whether the limit has improved ($y < 1$) or deteriorated ($y > 1$) in comparison to the reference limit.

A.8 $\Delta R_{\text{lep, lep}}$ COLL Limit Plots

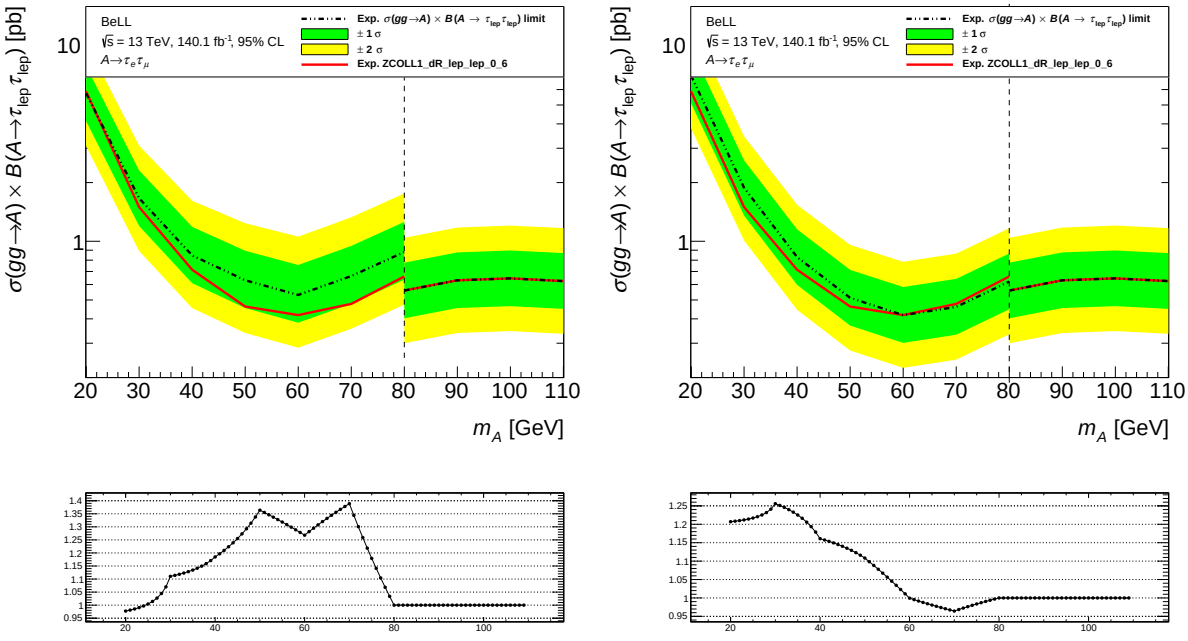

(a) (b)

Figure A.8: Upper limits of the $\Delta R_{\text{lep,lep}} < 0.4$ cut (A.8a) and the $\Delta R_{\text{lep,lep}} < 0.8$ cut (A.8b) on the $gg \to A$ production cross-section times the branching ratio for an A boson decay into two τ-leptons, which further decay into a μe, $\mu\mu$ or ee final state for A boson masses from 20 to 80 GeV. The dash-dotted line shows limit with the cuts and with its 1σ and 2σ uncertainty bands in green and yellow. The solid red line shows the limit of the chosen $\Delta R_{\text{lep,lep}} < 0.6$ cut (reference). The vertical dashed line indicates the splitting of the SR: only the low-mass hypotheses on the left side are being cut optimized in this work. The ratio plot beneath the limit plot shows the improvement or the deterioration of the limit (dashed line) in comparison to the reference (red line). The y-axis is plotted as: ratio $= \frac{\text{limit}}{\text{reference}}$, with $y = 1$ being the perfect agreement between the limit with the additional cut and the reference. The deviations of 1 indicate whether the limit has improved ($y < 1$) or deteriorated ($y > 1$) in comparison to the reference limit.

List of Figures

List of Tables

Selbstständigkeitserklärung

Hiermit erkläre ich, Jakob Walter, dass ich die vorliegende Arbeit „Kinematic Studies in the Search for a Low-Mass CP-Odd Higgs Boson for Mass Hypotheses in the Range from 20 GeV to 80 GeV“ selbstständig angefertigt und keine anderen als die angegebenen Hilfsmittel verwendet habe. Sämtliche wissentlich verwendete Textausschnitte, Zitate oder Inhalte anderer Verfasser wurden als solche gekennzeichnet.

Radebeul, den 20.12.2024

Jakob Walter